POLITECNICO DI TORINO
Repository ISTITUZIONALE

A Unified Approach for the Design of Accurate Torque Controllers for Electrically Excited Synchronous Motors

Original
A Unified Approach for the Design of Accurate Torque Controllers for Electrically Excited Synchronous Motors / Ionta, A., Rubino, S., Graffeo, F., Stella, F., Bojoi, R.. - In: IEEE TRANSACTIONS ON INDUSTRY APPLICATIONS. - ISSN 0093-9994. - (2026), pp. 1-21. [10.1109/tia.2026.3683647]

Availability:
This version is available at: 11583/3009848 since: 2026-04-14T07:59:15Z

Publisher:
IEEE

Published
DOI:10.1109/tia.2026.3683647

Terms of use:

This article is made available under terms and conditions as specified in the corresponding bibliographic description in the repository

Publisher copyright
IEEE postprint/Author's Accepted Manuscript

©2026 IEEE. Personal use of this material is permitted. Permission from IEEE must be obtained for all other uses, in any current or future media, including reprinting/republishing this material for advertising or promotional purposes, creating new collecting works, for resale or lists, or reuse of any copyrighted component of this work in other works.

(Article begins on next page)

15 November 2026

A Unified Approach for the Design of Accurate Torque Controllers for Electrically Excited Synchronous Motors

Alessandro Ionta, *Student Member, IEEE*, Sandro Rubino, *Senior Member, IEEE*, Federica Graffeo, *Member, IEEE*, Fausto Stella, *Member, IEEE* and Radu Bojoi, *Fellow, IEEE*

***Abstract*—Permanent magnet synchronous machines (PMSMs) with rare-earth magnets are widely recognized as the preferred choice for electric powertrains due to their high torque density and efficiency. However, in an effort to reduce reliance on rare-earth materials, electrically excited synchronous machines (EESMs) have emerged as a promising alternative for automotive applications. EESMs offer enhanced control flexibility over PMSMs, as their magnetic flux can be actively regulated through the rotor field current. The existing literature provides several torque control solutions for EESM, such as direct current control of the machine's currents and hybrid solutions that directly control the stator flux amplitude and torque. These torque control approaches (TCA) seem to lead to very different control structures, requiring a case-by-case design. However, this article proposes a unified approach specifically designed for traction EESMs that enables selecting the most common TCA reported in the literature while preserving accurate torque regulation and minimizing total copper loss. The effectiveness of the proposed solution is experimentally validated using a commercially available 100 kW EESM, which is employed in the Renault Zoe EV R135.**

***Index Terms*—electrically excited synchronous machine, traction, electric vehicles, torque control.**

I. Introduction

THE increased adoption of hybrid and electric traction powertrains has heightened the need for high-performance electrical machines at acceptable cost. The actual state-of-the-art identifies in permanent magnet synchronous machines (PMSMs) as the most widely used solution for electric powertrains, thanks to their high power and torque density [1]. However, the reliance on rare-earth materials presents challenges related to cost volatility, supply chain stability, and environmental sustainability. Consequently, alternative motor technologies that eliminate the need for permanent magnets have been investigated. The electrically excited synchronous machine (EESM) has been identified as a viable alternative topology for traction applications, owing to its ability to operate without magnets. Indeed, the EESM generates its excitation field through a dc winding in the rotor. Furthermore, this design inherently eliminates the risks associated with demagnetization and uncontrolled generation, both of which constitute potential failure modes in PMSMs. Moreover, the EESM provides greater control flexibility, as its magnetic flux can be actively regulated by adjusting the rotor field current. This capability facilitates extended constant power operation over a wide speed range while maintaining high efficiency and excellent flux-weakening performance [2]. As a result, numerous automotive manufacturers are increasingly considering EESMs as a viable alternative to PMSMs and are actively exploring various EESM topologies for traction applications [3]–[5].

However, effective torque control in EESMs involves addressing several control-related challenges [6]. One of the fundamental issues is the magnetic interaction between the stator d-axis and the rotor excitation system, which introduces coupling effects that complicate independent current control and necessitate the deployment of advanced, high-accuracy control algorithms [7]. In traction applications, EESMs are typically designed such that the exciter winding exhibits much higher inductance than the stator windings. This design characteristic results in a significantly slower dynamic response in the excitation circuit, even when the excitation system operates at its maximum voltage, compared to the relatively fast dynamics of the stator currents. Furthermore, maintaining operation along optimal efficiency trajectories requires frequent adjustments to the exciter current, further constraining the torque response capabilities of the system [8]. To partially mitigate these limitations, thermal management strategies can be employed to temporarily increase the allowable stator current during transient events, thereby enabling short-term overload operation. This enables the system to exploit the faster stator dynamics to enhance torque responsiveness under dynamic conditions [9]. Nonetheless, for a control solution that is both generalizable and robust, it is essential to leverage the magnetic coupling between stator and rotor fields [10].

The current state of research in ac drive control for traction applications identifies several well-established torque control approaches (TCAs). Among these, current vector control (CVC) [11]–[15] regulates torque by controlling the dq-components of the stator current vector (i_d, i_q). Direct torque control (DTC) [16], [17], particularly considering when combined with PWM modulation, achieves torque regulation by directly manipulating the stator flux amplitude and torque $(\hat{\lambda}, \hat{T})$. Direct flux vector control (DFVC) [18]–[20] blends the advantages of CVC and DTC by regulating torque through direct control of the stator flux amplitude and torque-producing current $(\hat{\lambda}, i_{qs})$. More recently, flux polar control (FPC) [21] has been introduced as a control methodology that regulates both the amplitude and load angle of the stator flux vector $(\hat{\lambda}, \hat{\delta})$, offering independence from machine inductances. Similarly, flux vector control (FVC) produce torque by managing

the dq-components of the stator flux vector $(\hat{\lambda}_d, \hat{\lambda}_q)$ [22].

Despite the above-mentioned extensive research on ac drive control strategies, few studies have explicitly focused on torque control for EESMs, with most implementations relying on dq current control [6], [8], [9], [23]–[25]. A more detailed analysis of EESM torque control is presented in [26], where a CVC scheme is discussed in stator dqs coordinates. In [27] and [28], a deadbeat-direct torque and flux control strategy is proposed, wherein a field flux linkage command is designed to achieve unity displacement power factor in steady-state conditions. However, since machine losses are not necessarily minimized at unity power factor, further optimization algorithms are required to enhance overall efficiency [8], [9], [24], [25], [29]–[31]. Coherently, a DFVC scheme incorporating a total copper loss-minimizing algorithm has been proposed in [32].

Each of the above-mentioned torque controllers leads to a specific design and control structure. Therefore, it seems that torque controllers for EESMs require a case-by-case design according to the selected TCA. However, the literature on PMSM's torque control demonstrates that it is possible to define unified control structures [12], [33] that can be adapted to implement the most common TCAs for motor drives. In other words, the literature does not report any control structure for EESM that can straightforwardly implement most of the control strategies reported in the literature, by using a unified approach based on generalized control maps.

Building on this research context, this article proposes one of the first torque controllers for traction EESMs that unifies the most common TCAs reported in the literature. The TCAs considered in this article are all based on the implementation of standard proportional-integral (PI) regulators, as they are the most widely employed solution in the automotive industry and offer straightforward code certification. Nonetheless, the proposed control structure allows implementing alternative regulators reported in the literature, such as dead-beat, model-predictive control, and sliding-mode, which are, however, outside the aim of this article. Among the possible TCAs, both rotor- and stator-flux-oriented solutions have been considered. In detail, among TCAs based on the rotor coordinates dq, CVC (i_d, i_q) and FVC (λ_d, λ_q) solutions have been considered. In parallel, regarding TCAs based on the stator coordinates (dqs), hybrid solutions like PWM-DTC (λ, T), DFVC (λ, i_{qs}), and FPC (λ, δ) have been considered. It is highlighted that for all these solutions, the optimal rotor current i_f control has been included.

According to the aim of this article, one of the most evident challenges is to guarantee accurate torque regulation when dealing with highly saturated EESMs, which are widely employed in traction applications. In addition, torque regulation accuracy must be combined with the aim of minimizing the overall EESM losses, i.e., copper and iron losses. Since iron losses are in many cases unknown or affected by high uncertainty, this article focuses on the overall copper-losses minimization (stator and rotor winding losses).

In summary, this article contributes to the literature by bringing the following added values.

- A torque controller dedicated to EESM that is able to unify the most common torque control approaches that are reported in the literature is proposed. All possible torque control approaches based on simple PI controllers are described with a survey approach, allowing any reader to properly select the best TCA, according to the application requirements and EESM characteristics. According to the authors' best knowledge, the literature lacks in survey papers describing properly different TCAs for EESM for traction applications.
- For the first time, a comprehensive procedure for computing and normalizing the control maps of saturated EESMs for traction applications is presented. Having as inputs the reference torque T^*, the reference machine flux λ^* and the field current i_f, the control maps are computed as look-up tables (LUTs) providing as output the controlled variables (currents or flux) according to the chosen TCA.
- The performance of all TCAs is evaluated through experiments conducted on a commercial EESM for electric vehicles, enabling a clear comparison of their performance under steady-state and transient operating conditions.

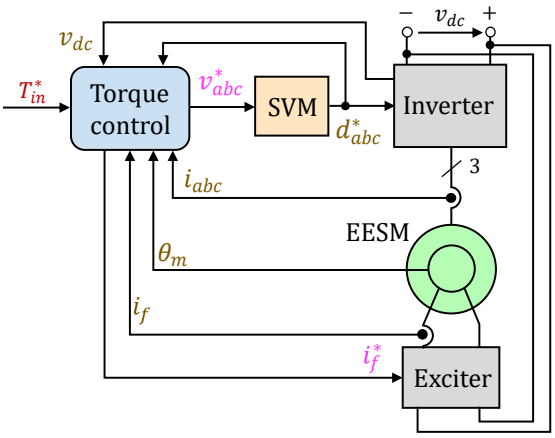


Fig. 1: Schematic view of EESM drive topology.

This article builds upon [34], where the proposed torque controller has been preliminarily validated at low speed. This article extends [34] by incorporating the following key aspects.

- Comprehensive description regarding the computation, normalization, and interpolation of proposed LUTs employed for guaranteeing accurate and efficient torque control is provided.
- Experimental validation of the proposed torque controller is conducted under high-speed operating conditions, comprising deep flux-weakening (FW) region with maximum torque per voltage (MTPV) limitation. Furthermore, a detailed analysis of the accuracy and achievable dynamic performance for each of the implemented TCA is provided.

As shown in Fig. 1, the EESM is fed on the stator by the inverter and on the rotor by an exciter. The torque control scheme generates the reference voltages v^*_{abc} for the inverter duty-cycle generation, along with the reference field current i^*_f for the exciter. Experimental results are provided for a commercial 100 kW EESM used on the Renault Zoe EV R135. The article is organized as follows. Section II presents the

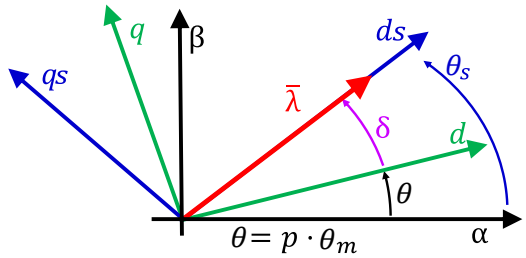


Fig. 2: Schematic view of the stationary- $\alpha\beta$, rotor- dq, and stator- dqs frames for a generic synchronous motor.

machine modeling in different reference coordinates with the theoretical background. A detailed description of the structure of the proposed torque controller is provided in Section III, while Section IV reports the experimental validation. Finally, Section V concludes the article.

II. EESM MODELING

EESMs can be modeled in both the rotor dq and stator dqs reference frames. In the stator frame, the ds-axis aligns with the stator flux linkage vector $\bar{\lambda}$, as shown in Fig. 2. The angular displacement between the stator flux and the rotor d-axis is referred to as the load angle δ.

Control strategies such CVC and FVC regulate stator current and stator flux, respectively, in the rotor dq frame. Alternatively, DTC, DFVC, and FPC operate in the stator dqs reference frame. Therefore, the electromagnetic equations and the state-space model in both dq and dqs coordinates are hereafter reported.

A. Electromagnetic model in rotor dq coordinates

The stator voltage equation in the rotor dq frame is expressed as in [35], extended including the rotor variables:

$$\bar{v}_{dq,f} = \begin{bmatrix} R & 0 & 0 \\ 0 & R & 0 \\ 0 & 0 & R_f \end{bmatrix} \cdot \begin{bmatrix} i_d \\ i_q \\ i_f \end{bmatrix} + \frac{\mathrm{d}}{\mathrm{dt}} \begin{bmatrix} \lambda_d \\ \lambda_q \\ \lambda_f \end{bmatrix} + \omega \cdot \begin{bmatrix} -\lambda_q \\ \lambda_d \\ 0 \end{bmatrix}, \quad (1)$$

where the subscripts of voltage v, current i, and flux linkage λ vectors indicate their respective components in the stator dq and rotor f reference frame, ω is the rotor synchronous speed.

The electromagnetic torque is given by:

$$T = \frac{3}{2} \cdot p \cdot \bar{\lambda} \times \bar{i} = \frac{3}{2} \cdot p \cdot (\lambda_d \cdot i_q - \lambda_q \cdot i_d), \quad (2)$$

where p is the pole pairs number.

To establish an explicit relationship between the stator voltage components expressed in the dq reference frame and the chosen state variables, it is necessary to derive the corresponding state–space equations. Within the framework of CVC strategies, torque regulation is achieved by directly manipulating the dq components of the stator current vector. The concept of differential inductances is introduced to locally formulate the state-space equations associated with the dq current dynamics. These inductances represent the partial derivatives of the stator flux linkages with respect to the stator and rotor currents and allow for a linearized representation of the machine's electromagnetic behavior around a specific operating point. The same concept is applied to define the state-space equation of the rotor current. Starting from the definition of differential inductances for PMSM included in [36], for EESMs, they are defined as follows:

$$[l_{dq,f}] = \begin{bmatrix} l_{dd} & l_{dq} & l_{df} \\ l_{qd} & l_{qq} & l_{qf} \\ l_{fd} & l_{fq} & l_{ff} \end{bmatrix} = \begin{bmatrix} \frac{\partial \lambda_d(i_d,i_q,i_f)}{\partial i_d} & \frac{\partial \lambda_d(i_d,i_q,i_f)}{\partial i_q} & \frac{\partial \lambda_d(i_d,i_q,i_f)}{\partial i_f} \\ \frac{\partial \lambda_q(i_d,i_q,i_f)}{\partial i_d} & \frac{\partial \lambda_q(i_d,i_q,i_f)}{\partial i_q} & \frac{\partial \lambda_q(i_d,i_q,i_f)}{\partial i_f} \\ \frac{\partial \lambda_f(i_d,i_q,i_f)}{\partial i_d} & \frac{\partial \lambda_f(i_d,i_q,i_f)}{\partial i_q} & \frac{\partial \lambda_f(i_d,i_q,i_f)}{\partial i_f} \end{bmatrix}. \quad (3)$$

It is important to highlight that in the formulation above, the inductances in the dq, f reference frame are not solely functions of the stator current components (i_d, i_q), but also exhibit a strong dependency on the rotor field current i_f. This dependence must be appropriately accounted for in the derivation of accurate machine models and in the implementation of advanced control strategies. This way, the cross-coupling between stator and rotor is fully accounted for. Exploiting (3), the stator voltage equation (1) becomes:

$$\bar{v}_{dq,f} = \begin{bmatrix} R & 0 & 0 \\ 0 & R & 0 \\ 0 & 0 & R_f \end{bmatrix} \cdot \begin{bmatrix} i_d \\ i_q \\ i_f \end{bmatrix} + [l_{dq,f}] \cdot \frac{d}{dt} \begin{bmatrix} i_d \\ i_q \\ i_f \end{bmatrix} + \omega \cdot \begin{bmatrix} -\lambda_q \\ \lambda_d \\ 0 \end{bmatrix}. \quad (4)$$

Performing some manipulations on (4), the state-space equations of the stator dq and rotor currents in a generic machine's operating point are computed as follows:

$$\begin{cases} l_{eq,d} \cdot \frac{d}{dt} i_d = (v_d - R \cdot i_d + \omega \cdot \lambda_q) - \\ k_{dq} \cdot (v_q - R \cdot i_q - \omega \lambda_d) + k_{df} \cdot (v_f - R_f \cdot i_f) \\ l_{eq,q} \cdot \frac{d}{dt} i_q = (v_q - R \cdot i_q - \omega \cdot \lambda_d) - \\ k_{qd} \cdot (v_d - R \cdot i_d + \omega \lambda_q) - k_{qf} \cdot (v_f - R_f \cdot i_f) \\ l_{eq,f} \cdot \frac{d}{dt} i_f = (v_f - R_f \cdot i_f) + \\ k_{fd} \cdot (v_d - R \cdot i_d + \omega \lambda_q) - k_{fq} \cdot (v_q - R \cdot i_q - \omega \cdot \lambda_d) \end{cases}, \quad (5)$$

where the terms indicated with k denote the cross-coupling factors that quantify the influence of the interactions between the axes and are defined as:

$$\begin{cases} k_{dq} = \frac{l_{qd} \cdot l_{ff} - l_{qf} \cdot l_{fd}}{l_{qq} \cdot l_{ff} - l_{qf} \cdot l_{fq}}; & k_{df} = \frac{l_{qd} \cdot l_{fq} - l_{qq} \cdot l_{fd}}{l_{qq} \cdot l_{ff} - l_{qf} \cdot l_{fq}}; \\ k_{qd} = \frac{l_{dq} \cdot l_{ff} - l_{df} \cdot l_{fq}}{l_{dd} \cdot l_{ff} - l_{df} \cdot l_{fd}}; & k_{qf} = \frac{l_{dd} \cdot l_{fq} - l_{dq} \cdot l_{fd}}{l_{dd} \cdot l_{ff} - l_{df} \cdot l_{fd}}; \\ k_{fd} = \frac{l_{dq} \cdot l_{qf} - l_{df} \cdot l_{qq}}{l_{dd} \cdot l_{qq} - l_{dq} \cdot l_{qd}}; & k_{fq} = \frac{l_{dd} \cdot l_{qf} - l_{df} \cdot l_{qd}}{l_{dd} \cdot l_{qq} - l_{dq} \cdot l_{qd}}; \end{cases} \quad (6)$$

while $l_{eq,d}$, $l_{eq,q}$ and $l_{eq,f}$ are the equivalent differential inductances along the corresponding axes and computed as:

$$\begin{cases} l_{eq,d} = l_{dd} - l_{dq} \cdot k_{dq} + l_{df} \cdot k_{df} \\ l_{eq,q} = l_{qq} - l_{qd} \cdot k_{qd} - l_{qf} \cdot k_{qf} \\ l_{eq,f} = l_{ff} + l_{fd} \cdot k_{fd} - l_{fq} \cdot k_{fq}. \end{cases} \quad (7)$$

The cross-coupling factors k_{dq}, k_{df}, k_{qd} and k_{qf} can frequently be neglected, as their effect on the system dynamics is minor and does not significantly impact the overall model accuracy in most practical cases. However, it is highlighted

that applying this simplification does not decouple the stator and rotor systems. Indeed, their correlation is still considered; as shown in (3), the differential inductances are functions of the instantaneous values of the d and q stator currents and the rotor current i_f. This reasoning cannot be applied to the rotor equation, where the cross-coupling factors k_{fd} and k_{fq} have a crucial role in the definition of the dynamic behavior of the rotor current i_f.

The cross-coupling terms act as an additive disturbance in the rotor control loop. For synchronous machines optimized for traction applications, the resistive voltage drops in the stator windings are often negligible due to their small relative magnitude.

Applying these simplifications and rearranging (5), the reduced-order state-space equations for the dq current dynamics can be written as:

$$\begin{cases} l_{dd} \cdot \frac{\mathrm{d}}{\mathrm{dt}} i_d \simeq v_d + \omega \cdot \lambda_q \\ l_{qq} \cdot \frac{\mathrm{d}}{\mathrm{dt}} i_q \simeq v_q - \omega \cdot \lambda_d \end{cases} . \tag{8}$$

The FVC regulates the dq flux components directly. The state-space equations for FVC have already been computed, as they correspond to (1).

$$\begin{cases} \frac{\mathrm{d}}{\mathrm{dt}} \lambda_d \simeq v_d + \omega \cdot \lambda_q \\ \frac{\mathrm{d}}{\mathrm{dt}} \lambda_q \simeq v_q - \omega \cdot \lambda_d \end{cases} . \tag{9}$$

The derived state-space equations can be used to systematically analyze the advantages and limitations of dq-based torque controllers. CVC's dependency on differential inductance requires adaptive regulators tuning, as also happens for the rotor current control. Conversely, the FVC is robust to variations in machine parameters and simplifies controller design. However, both CVC and FVC face challenges under voltage constraints in FW regions due to changing back-emf components ($\omega \cdot \lambda_q$ and $-\omega \cdot \lambda_d$) that couple the dq-axes significantly, making it necessary to adapt the voltage margins of the regulators since the prior control axis changes with the operating point according to the machine's load angle δ [21].

B. Electromagnetic model in stator dqs coordinates

The voltage model (10) and torque equation (11) are common to all ac machines in the stator flux frame as [18], [21], [32]:

$$\bar{v}_{dqs} = R \cdot \bar{i}_{dqs} + \frac{\mathrm{d}}{\mathrm{dt}} \cdot \begin{bmatrix} \lambda \\ 0 \end{bmatrix} + \lambda \cdot \begin{bmatrix} 0 \\ \omega + \frac{d\delta}{dt} \end{bmatrix}; \tag{10}$$

$$T = \frac{3}{2} \cdot p \cdot \bar{\lambda} \times \bar{i} = \frac{3}{2} \cdot p \cdot \lambda \cdot i_{qs}. \tag{11}$$

The rotor component is not reported as it is the same in every reference frame. Furthermore, the simplified model neglecting the cross-coupling factors k_{dq}, k_{df}, k_{qd} and k_{qf} is considered.

Equation (10) illustrates that the magnitude of the stator flux linkage λ can be effectively regulated by applying a control voltage component along the ds-axis. Concurrently, the qs-axis voltage component can be used to regulate the electromagnetic torque directly. DFVC, DTC and FPC exploit the direct relationship between the stator flux and the voltage components applied in the stator reference frame.

To establish a direct correlation between the dqs voltage components and the control variables employed in the DFVC (λ, i_{qs}), DTC (λ, T) and FPC (λ, δ) schemes, the corresponding state-space equations are derived and presented as follows. It is important to note that the state-space equation governing the stator flux amplitude has already been determined, as it corresponds to the ds-axis equation in (10).

$$\frac{\mathrm{d}\lambda}{\mathrm{dt}} = -R \cdot i_{ds} + v_{ds}. \tag{12}$$

The qs-axis voltage equation must be manipulated with a transformation of variables [21], and the final voltage model is described below.

$$l_{qs} \frac{di_{qs}}{dt} \simeq v_{qs} - \omega \cdot \lambda, \tag{13}$$

where :

$$l_{qs} = \frac{2 \cdot l_{dd} \cdot l_{qq}}{l_{dd} + l_{qq} - (l_{qq} - l_{dd}) \cdot \cos(2 \cdot \delta)}, \tag{14}$$

while l_{qs},l_{dd},l_{qq} are the equivalent differential inductances along the subscript axes.

Finally, the state-space equation of the torque is computed by applying the time derivative on (11) as [18]:

$$\begin{aligned} \frac{\mathrm{d}}{\mathrm{dt}} T = \frac{3}{2} \cdot p \cdot \left(\frac{\mathrm{d}}{\mathrm{dt}} \lambda \cdot i_{qs} + \lambda \cdot \frac{\mathrm{d}}{\mathrm{dt}} i_{qs} \right) \rightarrow \\ \frac{2 \cdot l_{qs}}{3 \cdot p \cdot \lambda} \cdot \frac{\mathrm{d}}{\mathrm{dt}} T \simeq v_{qs} - \omega \cdot \lambda. \end{aligned} \tag{15}$$

According to the machine model in the dqs coordinates, as detailed in equations (10), (11), and the corresponding state-space equations (12), (13), the benefits of the DFVC and DTC schemes become evident.

One of the main advantages is that torque regulation maintains its linearity across all operating conditions, including FW operations. Within DFVC schemes, the qs-axis current reference is directly derived from equation (11), based on a predetermined flux amplitude. This approach eliminates the need for LUTs for torque regulation's accuracy, which are typically required in LUT-based CVC solutions [18], [32]. This advantage is also evident in DTC schemes.

Moreover, beyond the base speed, the flux amplitude reference can be effectively constrained using model-based laws that remain unaffected by magnetic saturation phenomena. This capability enables the straightforward implementation of the FW. The dynamic performance of the closed-loop control of the stator flux amplitude remains invariant across varying machine's operating points, as indicated by equation (12).

A further advantage of DFVC and DTC is that the inner regulators for flux amplitude and the qs-axis current operate with independent voltage margins. Only a minimal voltage margin is needed to counteract the voltage drops in the ds-axis due to stator resistance and the inverter voltage errors. As a result, the qs-axis regulator can utilize nearly the full voltage range supplied by the inverter, ensuring exceptionally high dynamic performance of torque regulation even under voltage constraints [18].

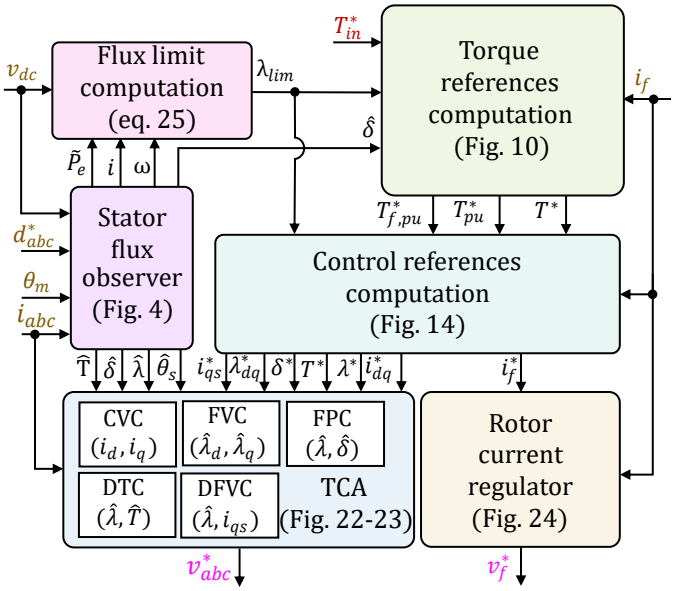


Fig. 3: Schematic view of the proposed torque controller.

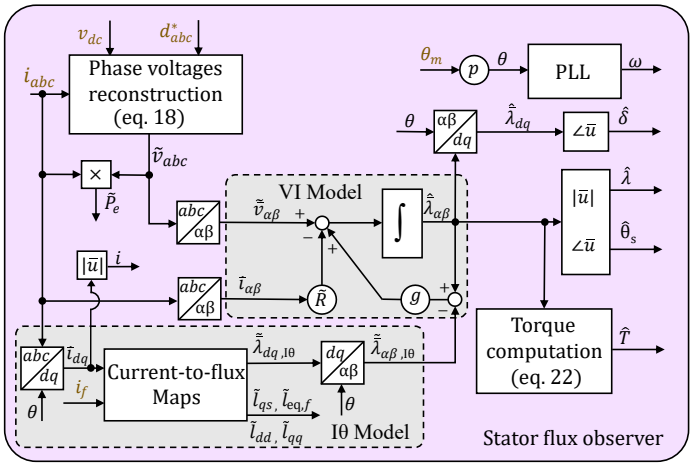


Fig. 4: Schematic view of the adopted stator flux observer.

The FPC-based torque controller performs torque regulation by directly controlling the stator flux vector in terms of amplitude λ and load angle δ. The qs-axis voltage is used to perform the closed-loop control of the machine's load angle δ. Therefore, the corresponding state-space equation is obtained from (10) as follows.

$$\lambda \cdot \frac{\mathrm{d}}{\mathrm{dt}}\delta \simeq v_{qs} - \omega \cdot \lambda. \tag{16}$$

The FPC scheme provides the previously described advantages of DTC and DFVC solutions. Additionally, as shown in equation (16), the performance of the load angle control loop is independent of the magnetic saturation. However, the FPC scheme does not automatically guarantee the accuracy of torque regulation, unlike DTC and DFVC solutions. Indeed, the load angle cannot be directly correlated to the torque using analytical relationships due to the influence of magnetic saturation. Therefore, a LUT is required to provide the load angle reference.

III. Torque Control Scheme

The schematic representation of the proposed torque controller is illustrated in Fig. 1 and Fig. 3.

Based on the input torque reference T^*_{in}, the controller computes the reference stator phase voltages $v^*_{abc} = [v^*_a, v^*_b, v^*_c]$ and the reference rotor voltage v^*_f. These outputs are generated by processing several feedback signals, including the stator phase currents $i_{abc} = [i_a, i_b, i_c]$, the inverter dc-link voltage v_{dc}, the rotor mechanical position θ_m, and the rotor field current i_f. Subsequently, the reference stator phase voltages are used to derive the inverter duty cycles $d^*_{abc} = [d^*_a, d^*_b, d^*_c]$ through the implementation of any PWM strategy [37]. In this work, a carrier-based space vector modulation (SVM) technique is adopted.

As shown in Fig. 3, the developed control structure implements the following control blocks:

A. Stator flux observer
B. Flux limit computation
C. Torque references computation
D. Control references computation
E. Torque control approach (TCA)
F. Rotor current regulator

A description of the aforementioned control modules is presented in the following sections, including a discussion on the implementation of LUTs required to derive the control references addressing the non-linear dependence of the EESM's magnetic behavior on the rotor current i_f.

Throughout the description of the control architecture, the following superscript are adopted: " ˜ " denotes an estimated quantity, " ˆ " indicates an observed quantity, and " * " represents a reference value. Estimated quantities arise from open-loop model propagation, while observed quantities are obtained from closed-loop observers incorporating measurement feedback.

A. Stator flux observer

The stator flux vector is estimated by adopting a consolidated flux observer structure [18], [38], [39] that combines two model-based estimators, see Fig. 4.

- The current model (Iθ) provides the flux estimate based on the current-to-flux relationships [18], implemented in the proposed control structure using LUTs. In the same way, the estimation of the differential inductances (3), (14) can be retrieved. Indeed, the current-to-inductance relationships are computed by processing the current-to-flux ones and stored in LUTs. The flux and inductance maps are shown in Figs. 5 - 9.
- The voltage model (VI) provides the flux estimate as the integral of the stator back-electromotive force voltage vector, where the voltages $\tilde{v}_{abc}$ are reconstructed from the measured inverter dc-link voltage and the command duty-cycles d^*_{abc} [39], [40]. Ideally, the reconstructed voltages are only function of the duty-cycles as:

$$\begin{bmatrix} \tilde{v}_{a,id} \\ \tilde{v}_{b,id} \\ \tilde{v}_{c,id} \end{bmatrix} = v_{dc} \cdot \begin{bmatrix} d^*_a - d_0 \\ d^*_b - d_0 \\ d^*_c - d_0 \end{bmatrix}, \quad d_0 = \frac{d^*_a + d^*_b + d^*_c}{3} \tag{17}$$

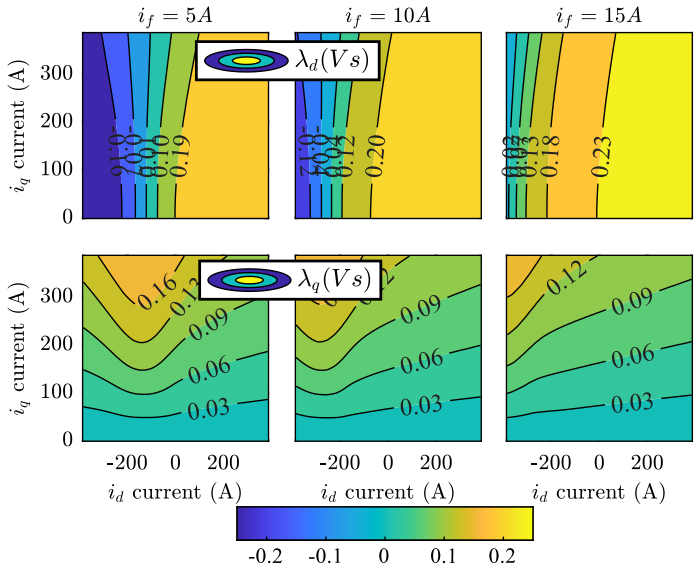


Fig. 5: Current-to-flux maps for the EESM under consideration.

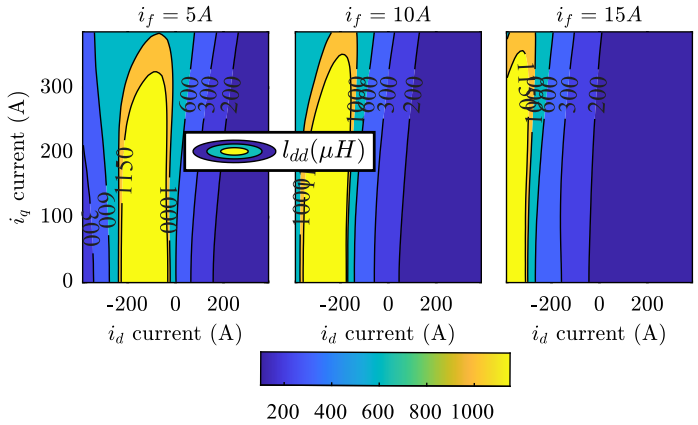


Fig. 6: Current-to-inductance l_{dd} map for the EESM under consideration.

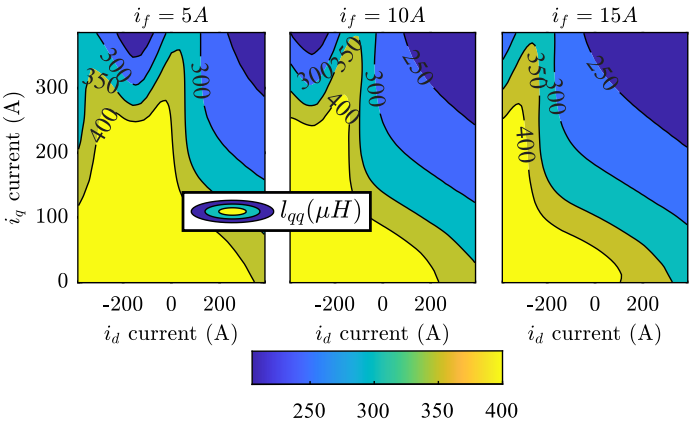


Fig. 7: Current-to-inductance l_{qq} map for the EESM under consideration.

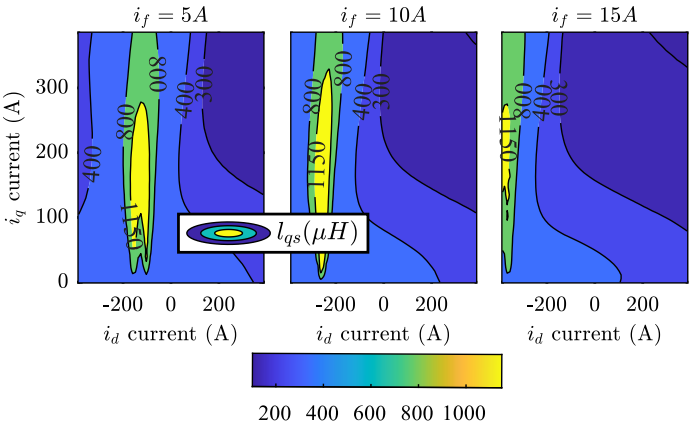


Fig. 8: Current-to-inductance l_{qs} map for the EESM under consideration.

However, the compensation for voltage errors $\tilde{v}_{dt,abc}$ introduced by the inverter non-idealities (dead-time effects and threshold voltages for IGBT implementations) is necessary to improve the observer's accuracy. The voltage errors $\tilde{v}_{dt,abc}$ can be evaluated using most of the solutions reported in the literature. In this work, the estimation method proposed in [40] has been implemented. Therefore, the stator voltages $\tilde{v}_{abc}$ are estimated as:

$$\tilde{v}_{abc} = \tilde{v}_{abc,id} - \tilde{v}_{dt,abc} - \tilde{R}_{VSI} \cdot i_{abc} \tag{18}$$

where $\tilde{R}_{VSI}$ is the equivalent resistance that accounts for the conduction voltage drops of the inverter switches.

Based on Fig. 4, the transition frequency between Iθ model, whose flux estimate is robust at low speed, and VI model, whose flux estimate is instead reliable at high speed, is established by the observer gain g. More details about the observer can be found in the literature [18], [38]–[40].

The observer outputs the following quantities:

- Flux amplitude

$$\hat{\lambda} = \sqrt{\hat{\lambda}_\alpha^2 + \hat{\lambda}_\beta^2}. \tag{19}$$

- Stator flux vector position

$$\hat{\theta}_s = \text{atan2}\left(\frac{\hat{\lambda}_\beta}{\hat{\lambda}_\alpha}\right). \tag{20}$$

- Load angle

$$\hat{\delta} = \text{atan2}\left(\frac{\hat{\lambda}_q}{\hat{\lambda}_d}\right). \tag{21}$$

- Observed torque

$$\hat{T} = \frac{3}{2} \cdot p \cdot (\hat{\lambda}_\alpha \cdot i_\beta - \hat{\lambda}_\beta \cdot i_\alpha). \tag{22}$$

In addition, although not directly obtained by the flux observer, the following quantities are computed since several control modules of the proposed torque controller require them.

- Estimated electric power

$$\tilde{P}_e = (\tilde{v}_a \cdot i_a + \tilde{v}_b \cdot i_b + \tilde{v}_c \cdot i_c). \tag{23}$$

- Current amplitude

$$i = \sqrt{i_d^2 + i_q^2}. \tag{24}$$

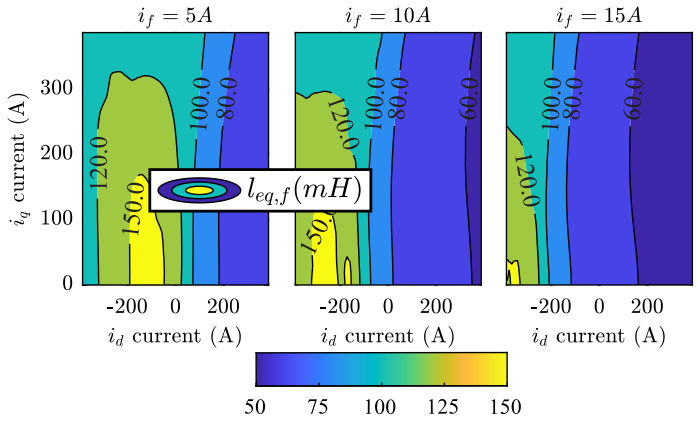


Fig. 9: Current-to-inductance $l_{eq,f}$ map for the EESM under consideration.

Finally, the electric speed ω can be computed using a phase-locked loop (PLL) [41], whose input is the d-axis position that is obtained from the measured mechanical position θ_m.

B. Flux limit computation

The design of the torque control algorithm must rigorously account for the operational constraints imposed by the electrical machine as well as the power electronics converters supplying it, specifically the inverter and the exciter. These constraints are essential to ensure safe and efficient operation under all conditions. As previously discussed, EESMs introduce the rotor field current i_f as an additional controllable variable. This added degree of freedom necessitates the inclusion of an additional constraint on the maximum permissible rotor current, denoted as $i_{f,\max}$, alongside the conventional stator current limit $i_{\max}$.

Furthermore, in the FW operating region, it becomes crucial to limit the flux amplitude λ to prevent violating the voltage constraint. As the rotor speed increases, the maximum allowable flux $\lambda_{\lim}$ must be dynamically adjusted based on the inverter's maximum output voltage capability. This limitation is computed using the expression given in (25), which also incorporates the effects of resistive voltage drops in the stator windings [21].

$$\lambda_{\lim} = k_{fw} \cdot \frac{\sqrt{v_{\max}^2 + (\tilde{R} \cdot i)^2 - (4/3) \cdot \tilde{R} \cdot \tilde{P}_e}}{|\omega|}. \tag{25}$$

In (25), v_{max} represents the maximum allowable phase voltage, corresponding to the sinusoidal voltage limit of the inverter. Since SVM is employed, this limit is given by $v_{dc}/\sqrt{3}$. The parameter k_{fw} is a scaling factor introduced to account for inverter non-idealities and to provide a safety margin that ensures robust dynamic performance during torque control, particularly in deep FW conditions. Typical values for k_{fw} range from 0.9 to 0.95.

It is important to note that the flux limit λ_{lim} must always remain below or equal to the machine's intrinsic maximum flux capability, denoted as λ_{max}, which is determined by the machine's current-to-flux characteristics.

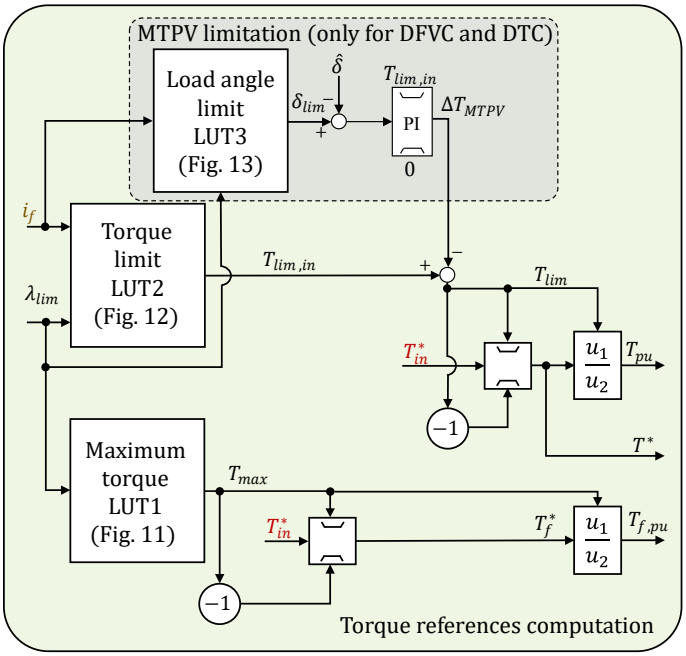


Fig. 10: Schematic view of the torque references computation.

In summary, flux and current limitations correspond to the following constraints:

$$\begin{cases} i \le i_{\max} \\ i_f \le i_{f,\max} \\ \lambda \le \lambda_{\lim} \le \lambda_{\max} \end{cases}. \tag{26}$$

C. Torque references computation

As previously noted, a significant limitation in controlling traction EESMs comes from the slow dynamic response of the excitation system. This behavior is primarily due to the inherently high inductance of the rotor winding, which significantly limits the rate of change of the rotor current i_f.

The stator currents respond much more rapidly than the rotor current to a step variation. Therefore, to address this challenge, two distinct torque references are introduced:

1) T_f^*: torque reference for the rotor current regulation;
2) T^*: torque reference for the stator quantities regulation.

The corresponding control structure, illustrated in Fig. 10, enables high-performance torque control even in the presence of slow exciter dynamics. It is highlighted that this dual-torque-reference mechanism is not strictly required for standard traction cycles, as the dynamic variations in torque requests are typically slow. However, the dual-torque-reference is recommended for EESM with a large rotor time constant and the need for executing rapid torque transients. In detail, two possible scenarios with a unified torque reference, along with their criticality, are identified and reported hereafter.

- The stator torque reference T^* is utilized to derive the rotor and stator reference quantities. The rotor current reference generation becomes inconsistent because it depends on a torque reference that is itself limited by the

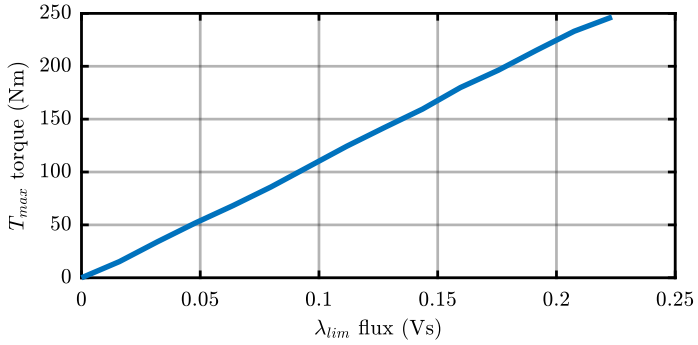


Fig. 11: Maximum torque profile (LUT1) for the EESM under consideration.

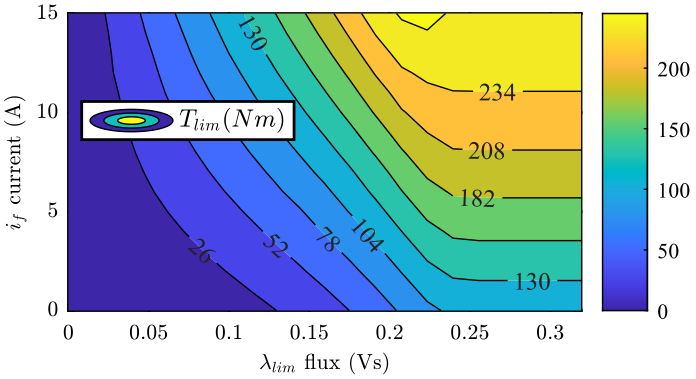


Fig. 12: Torque limit map (LUT2) for the EESM under consideration.

rotor current. This loop further reduces the dynamic of the rotor current regulation.

- The rotor torque reference T_f^* is directly utilized to derive the rotor and stator reference quantities. While the rotor current control loop operates normally in this scenario, significant damping issues may arise in the generation of stator references whenever the actual rotor current i_f deviates significantly from its reference i_f^*. This discrepancy is particularly critical during fast torque transients.

1) Torque reference for rotor current regulation: The rotor-side torque reference T_f^* is computed by first determining the maximum torque T_{max} that the machine can produce, taking into account the instantaneous limitations imposed by the flux amplitude limit λ_{lim} (derived from voltage constraints), and the fixed stator and rotor maximum currents ($i_{\text{max}}, i_{f,\text{max}}$).

The maximum torque T_{max} is obtained through interpolation of the pre-elaborated one-dimensional LUT1. Fig. 11 provides a visualization of the maximum torque T_{max} profile.

Once T_{max} is known, the rotor torque reference T_f^* is obtained by limiting the input torque request T_{in}^* as:

$$|T_f^*| = \min\left(|T_{\text{in}}^*|, |T_{\text{max}|}\right). \tag{27}$$

It is highlighted that this torque limitation primarily reflects the limitations of the stator-side by including λ_{lim}, and does not explicitly incorporate the dynamics of the rotor current i_f.

2) Torque reference for stator quantities regulation: The stator torque reference T^* must be compatible with both the instantaneous rotor current value i_f and the operational safety constraints of the machine (26).

The first limitation involves computing an intermediate torque limit $T_{lim,in}$ that is compatible with the machine's actual operational state and is illustrated in Fig. 10. This limit is obtained via interpolation of the two-dimensional LUT2, whose inputs are the flux amplitude limit λ_{lim} and the measured rotor current i_f.

The torque limit $T_{lim,in}$ ensures that the stator can temporarily deliver higher current (up to i_{max}) to satisfy rapid torque demands. In contrast, the rotor current can slowly converge to its target value. This allows for dynamic performance improvements without violating converter or machine safety limits (26) and ensures that the desired efficiency strategy is applied at steady state.

However, in deep flux-weakening operation, MTPV conditions may arise. Under such conditions, DFVC and DTC schemes require an explicit limitation on the machine load angle δ to prevent instability and machine pull-out [18]. Although the limit $T_{lim,in}$ accounts for MTPV implicitly, additional regulation is needed to ensure that the estimated load angle $\hat{\delta}$ remains within the safe boundary defined by the critical angle δ_{lim} if DFVC or DTC schemes are implemented. For this purpose, an outer-loop proportional-integral (PI) controller is implemented to regulate $\hat{\delta}$ such that:

$$\hat{\delta} \leq \delta_{\text{lim}}. \tag{28}$$

To enable straightforward handling of both motoring and generating operations, $\hat{\delta}$ and δ_{lim} are both handled as absolute values. The critical load angle δ_{lim} is obtained through interpolation of the two-dimensional LUT3, using the flux amplitude limit λ_{lim} and the measured rotor current i_f, as input parameters. LUT3 for the considered EESM is shown in Fig. 13.

The output of the PI controller, denoted ΔT_{MTPV}, serves as a correction term of the torque limit $T_{lim,in}$ to ensure torque stability. However, this value is strictly bounded to ensure that the overall torque command remains within the machine's capabilities as:

$$T_{\text{lim}} = T_{\text{lim,in}} - \Delta T_{\text{MTPV}}, \quad \text{with} \quad \Delta T_{\text{MTPV}} \leq T_{\text{lim,in}}. \tag{29}$$

Finally, the stator-side torque reference T^* is obtained as depicted in Fig. 10 as:

$$|T^*| = \min\left(|T_{\text{in}}^*|, |T_{\text{lim}}|\right). \tag{30}$$

The proposed approach ensures that high-performance torque regulation is maintained across a wide range of operating conditions, including deep FW and MTPV limitation, while fully respecting the constraints of the EESM.

D. Control references computation

Starting from the stator torque reference T^*, the complete set of control references required for each TCA can be systematically derived, as shown in Fig. 14. These include the optimal stator flux amplitude λ^*, stator current dq components i_d^* and i_q^* for CVC, stator flux dq components λ_d^* and λ_q^* for FVC,

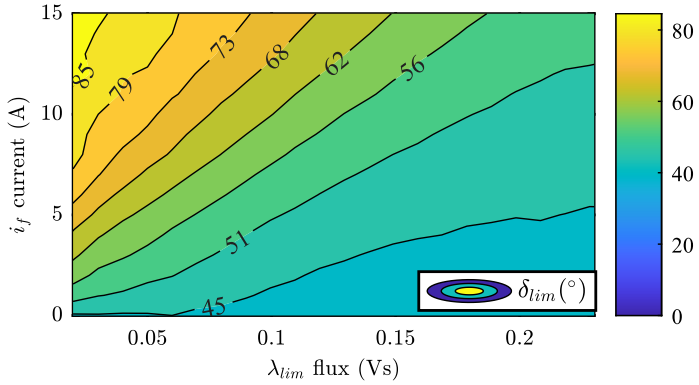


Fig. 13: Load angle limit map (LUT3) for the EESM under consideration.

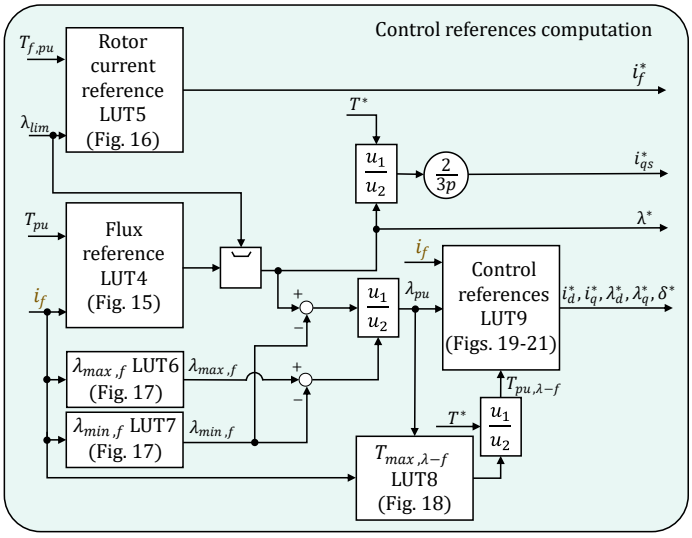


Fig. 14: Schematic view of the flux and currents references computation.

load angle reference δ^* for FPC, and stator torque-producing current i_{qs}^* for DFVC. Concurrently, the rotor current reference i_f^* is computed based on the rotor torque reference T_f^*.

It is important to note that multiple combinations of stator $(\bar{\lambda}, \bar{i})$ and rotor (i_f) control variables can yield the same torque output. This redundancy comes from the fact that torque generation for EESMs depends on the interaction between the stator and rotor quantities.

Moreover, for enhanced flexibility and performance, it is advantageous to decouple flux and torque control. This separation allows the flux reference to be optimized in the desired way independently of the instantaneous torque requirement.

1) Stator flux amplitude and rotor current references: Regardless of the adopted TCA, the optimal stator flux amplitude λ^* is computed in compliance with the current and voltage constraints defined in equation (26). This ensures that the resulting control references remain within the machine's safe operating limits.

Although any efficiency strategy can be employed in the proposed torque control scheme, in this article, the optimal references for stator flux amplitude λ^* and rotor current i_f^* are obtained by solving a constrained optimization problem that minimizes the total copper losses subject to the electrical limits expressed in equation (26):

$$\min_{\lambda, i_f} \left\{ \frac{3}{2} \cdot R \cdot i^2 + R_f \cdot i_f^2 \right\}. \tag{31}$$

The constrained minimization problem formulated in (31) poses significant challenges for its resolution, primarily due to the nonlinear magnetic behavior of EESMs, which is highly dependent on the rotor excitation current i_f. In particular, the machine's flux linkage characteristics exhibit strong saturation effects and cross-coupling phenomena, making real-time analytical solutions impractical.

To address this complexity, the optimization problem (31) is solved offline, exploiting FEA or experimentally derived current-to-flux maps of the EESM [42], [43]. By leveraging these nonlinear relationships, it is possible to pre-compute the optimal control variables that minimize the total copper losses under various operating conditions.

Specifically, two LUTs are generated:

- LUT4 provides the optimal stator flux amplitude reference λ^*,
- LUT5 provides the optimal rotor current reference i_f^*.

For both LUTs, the respective torque reference is correlated with the other input. Indeed, the rotor torque reference T_f^* is dependent on the flux amplitude limit λ_{lim}, while the stator torque reference T^* is dependent on the actual rotor current i_f. This mutual correlation between the input variables of LUT4 and LUT5 results in a highly irregular map domain, which poses challenges for implementing and interpolating these LUTs on digital controllers.

To efficiently address this issue, the method proposed in [21] is adopted. In the case where one or more input directions of the LUT are dependent on others, a normalization procedure is applied. Specifically, the dependent input dimensions are transformed into a per-unit (pu) scale ranging from 0 to 1. In this normalized domain:

- A value of 0 corresponds to the minimum physically admissible value of the variable for the given values of the other inputs.
- A value of 1 corresponds to its maximum admissible value of the variable for the given values of the other inputs.

This normalization ensures that the LUT can be interpolated with linear methods while preserving the integrity of the original nonlinear relationships.

Following these considerations, the linear interpolation of LUT4 and LUT5 requires the pu normalization of their respective torque references according to the corresponding maximum limits as (see Fig. 10):

$$T_{\text{pu}} = \frac{T^*}{T_{\text{lim}}}; \quad T_{f,\text{pu}} = \frac{T_f^*}{T_{\text{max}}}. \tag{32}$$

A view of the flux amplitude reference map (LUT4) is shown in Fig. 15 for different values of the measured rotor current i_f. A view of the rotor current reference map (LUT5)

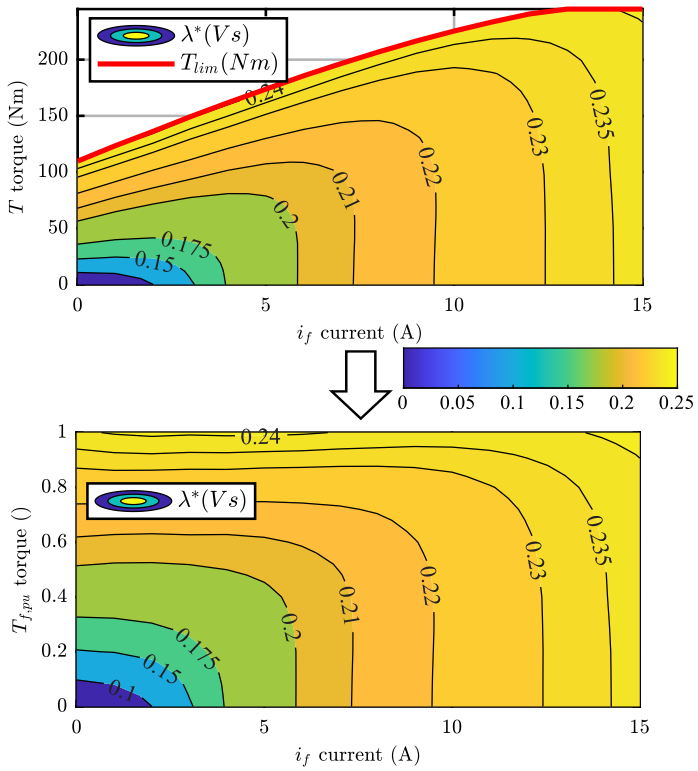


Fig. 15: Flux amplitude reference (λ^*) map (LUT4) for the EESM under consideration.

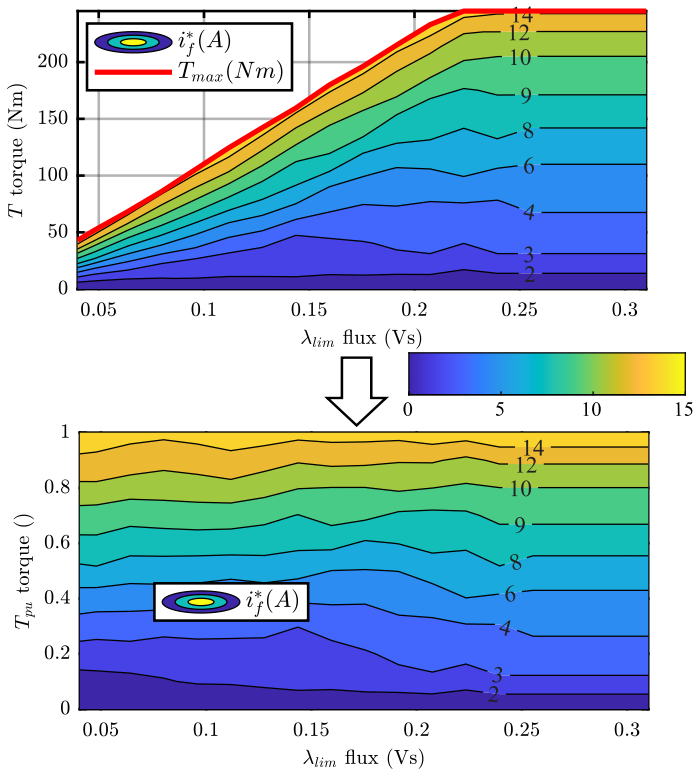


Fig. 16: Rotor current reference (i_f^*) map (LUT5) for the EESM under consideration.

is instead shown in Fig. 16 for different values of the flux amplitude limit λ_{lim}.

It is highlighted that LUT4 and LUT5 can be modified to implement alternative optimization strategies (e.g., minimization of Joule plus iron losses, including temperature effects on rotor and stator resistance and the electrical frequency) without changing the proposed control structure (see Fig. 3).

2) Computation of TCA references: As illustrated in Fig. 14, given the actual value of the rotor current i_f and the references of torque and stator flux amplitude (T^*, λ^*), it is possible to derive the reference quantities of any TCA $(i_d^*, i_q^*, \lambda_d^*, \lambda_q^*, \delta^*, i_{qs}^*)$. Except for the reference torque-producing current i_{qs}^*, which is calculated from (11), these reference quantities are ruled by non-linear relationships, requiring the adoption of LUT9, as depicted in Fig. 14.

The implementation of LUT9 on digital controllers is not straightforward. Indeed, both torque and flux amplitude depend on the rotor current i_f. In turn, the torque is also related to the flux amplitude. Therefore, one of the main contributions of this article is the definition of the procedure to normalize and interpolate LUT9 independently of the considered TCA, generalizing the concepts of the normalization procedure proposed in [21] for PMSMs.

First, the flux amplitude is normalized in pu form, in coherence with the actual rotor current i_f. Therefore, for each i_f, a minimum and a maximum flux are defined, $\lambda_{\text{min},f}$ and $\lambda_{\text{max},f}$ respectively. Such relationships are stored in LUT6 and LUT7 (see Fig. 17). Straightforwardly:

$$\lambda_{\text{pu}} = \frac{\lambda^* - \lambda_{\text{min},f}}{\lambda_{\text{max},f} - \lambda_{\text{min},f}}. \tag{33}$$

It is highlighted that the minimum flux $\lambda_{\text{min},f}$ is almost null for the considered EESM. However, different EESMs can exhibit a significant minimum flux $\lambda_{\text{min},f}$ characteristic, justifying the need for its elaboration.

Subsequently, a maximum torque $T_{\text{max},\lambda-f}$ expressed as a function of the i_f and the λ_{pu} is defined and stored in LUT8 (see Fig. 18). A new pu reference torque is thus retrieved as:

$$T_{\text{pu},\lambda-f} = \frac{T^*}{T_{\text{max},\lambda-f}}. \tag{34}$$

Finally, the desired control references can be found linearly interpolating LUT9, whose inputs are λ_{pu}, $T_{\text{pu},\lambda-f}$ and i_f. It is highlighted that the output of LUT9 changes according to the considered TCA, and that it is not required for DFVC and DTC schemes (see Figs. 19 - 21).

Summarizing, LUT4 and LUT5 are used to provide the optimal reference of stator flux λ^* and rotor current i_f^* according to the considered efficiency strategy (in this work, minimum copper losses) and the corresponding torque reference (T^*, T_f^*). This way, the stator and the rotor control are dynamically decoupled, allowing the overall torque control dynamic to be limited only by the stator dynamics and the machine's constraints (26). Subsequently, LUT9 is employed to derive the control references necessary to implement the desired TCA starting from the measured rotor current i_f and the references of stator flux amplitude λ^* and torque T^*.

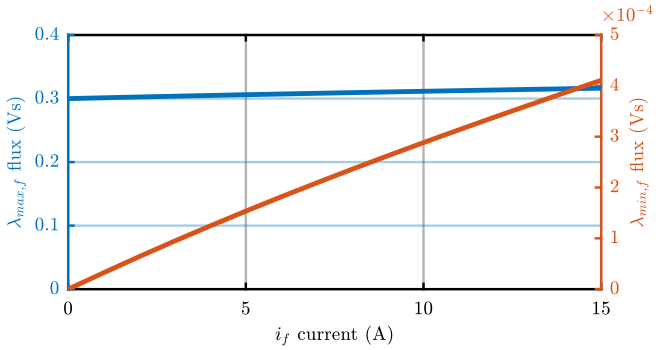


Fig. 17: Maximum and minimum flux as a function of the rotor current (LUT6 and LUT7) for the EESM under consideration.

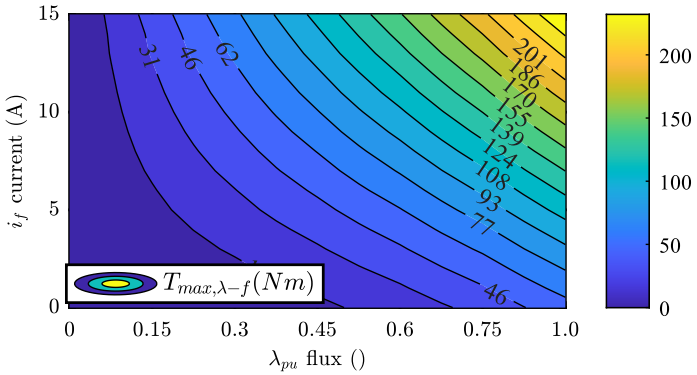


Fig. 18: Maximum torque map as a function of the rotor current and the stator flux amplitude (LUT8) for the EESM under consideration.

It is highlighted that the proposed control structure is quite robust against temperature effects. As the EESMs are magnetless, the current-to-flux and current-to-torque maps are independent of temperature, making LUT1-LUT3 and LUT6-LUT9 invariant to temperature variations. Conversely, LUT4 and LUT5 are computed according to the overall Joule losses minimization by considering rated temperature of stator and rotor windings. Therefore, these two LUTs should be adapted to the measured/estimated machine temperatures to preserve the minimum overall Joule losses conditions. However, torque accuracy is preserved because it relies only on LUT9.

E. Torque control approach (TCA)

The proposed torque controller can employ any desired TCA, which can be chosen based on specific application requirements and EESM design. Depending on the chosen TCA, different regulators' characteristics have been previously highlighted in Sections II-A and II-B and deeply analyzed in the following.

1) Stator dqs-axes TCAs: In the DFVC, DTC and FPC the torque control is performed using two regulators implemented in the stator dqs frame, as shown in the schematic view of Fig. 22.

As highlighted in Section II-B, only a minimal voltage is required by ds-axis/flux regulator to counteract the voltage drops attributable to the stator resistance and the inverter.

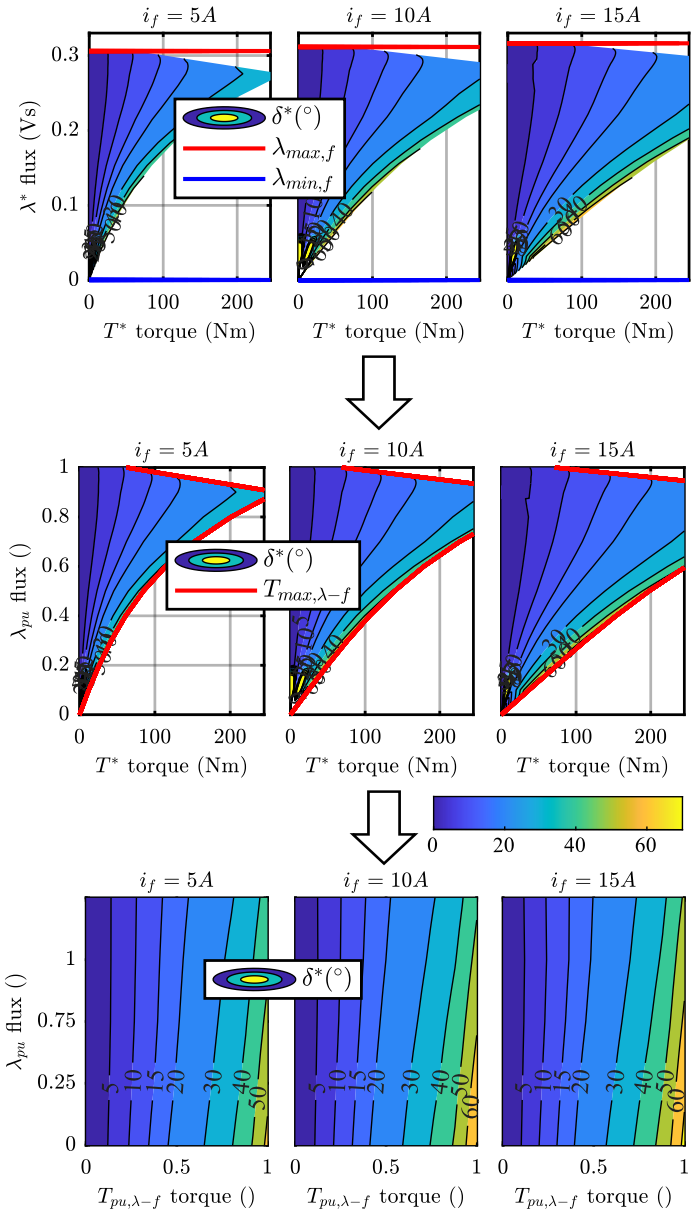


Fig. 19: Load angle reference (δ^*) normalization (LUT9) for the EESM under consideration.

Hence, the voltage margin for the flux amplitude regulation $v_{ds,lim}$ can be set following a rule of thumb law:

$$2 \cdot R \cdot i_{\max} \leq v_{ds,\lim} \leq 5 \cdot R \cdot i_{\max}. \tag{35}$$

This way, the qs-axis regulator, responsible for the torque-producing quantity $(i_{qs}, \hat{T}, \hat{\delta})$ regulation, can utilize nearly the full voltage range provided by the inverter, thereby enabling exceptionally high dynamic performance in torque regulation even in deep FW operation. To further improve the dynamic performance of torque regulation, the compensation of the machine's back-electromotive force $(\omega \cdot \hat{\lambda})$ is performed (see Fig. 22).

Recalling (12), it is evident that the performance of the flux regulator is independent of the machine's working point. Thus, if a PI flux regulator is applied, it does not need any tuning and proportional $-k_p$ and integral $-k_i$ gains are suggested to

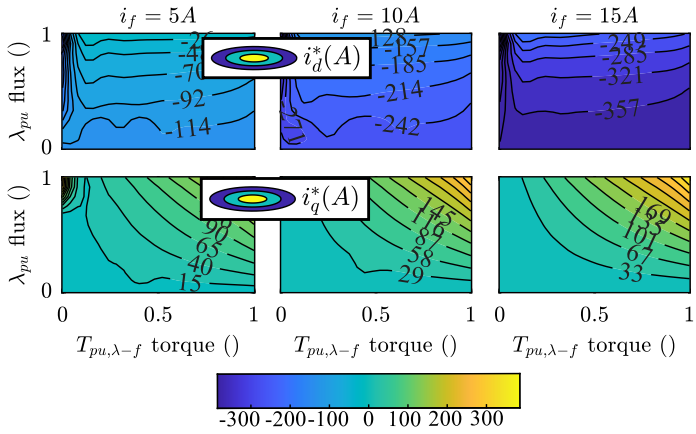


Fig. 20: dq currents references (i_d^*, i_q^*) normalization (LUT9) for the EESM under consideration.

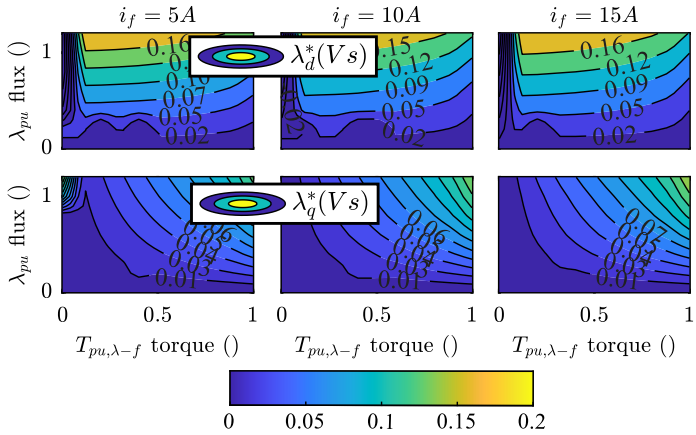


Fig. 21: dq stator fluxes references $(\lambda_d^*, \lambda_q^*)$ normalization (LUT9) for the EESM under consideration.

be designed as in [21]. The same happens for the load angle regulator, as evident from (16).

Conversely, the $\hat{T}$ and i_{qs} control loops, according to (13) and (15), are related to the machine magnetic saturation through the differential inductance l_{qs}. Therefore, the gains of the qs-axis regulator need to be dynamically adapted according to the estimation of the differential inductance $\tilde{l}_{qs}$, retrieved from the magnetic model in the flux observer, avoiding undamped or instability phenomena. More details about the preliminary computation of the PI gains for stator dqs-axes TCAs are reported in Appendix.

2) Rotor dq-axes TCAs: The CVC and FVC implement the closed-loop control of the stator dq-axes currents and fluxes, respectively. Therefore, the back-emf components $(-\omega \cdot \lambda_q$ and $\omega \cdot \lambda_d)$ must be compensated to obtain satisfactory performance in FW, as can be seen in Fig. 23. Recalling (8), it is evident that CVC requires adaptive regulators tuning according to the estimated differential inductances $\tilde{l}_{dd}$ and $\tilde{l}_{qq}$ (see Fig. 6 and Fig. 7). Conversely, according to (9), it is noted that the FVC regulators are both independent from the machine's operating point and can be tuned as for the flux amplitude regulator. More details about the preliminary computation of the PI gains for rotor dq-axes TCAs are reported in Appendix.

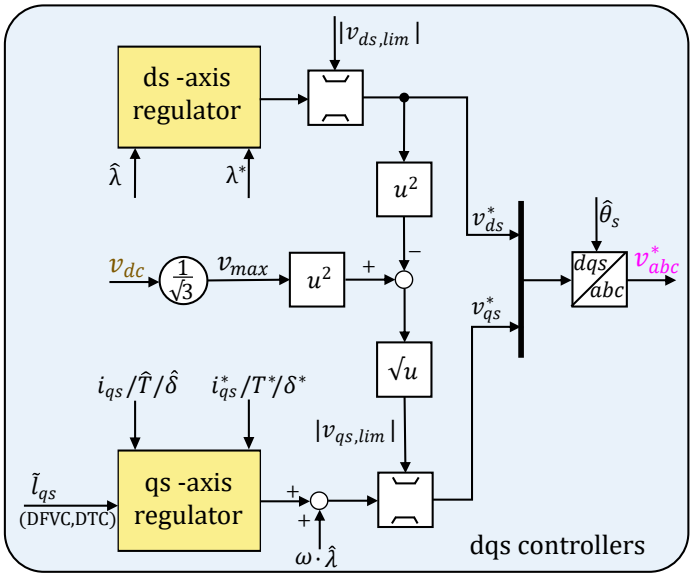


Fig. 22: Schematic view of the dqs-frame based TCAs.

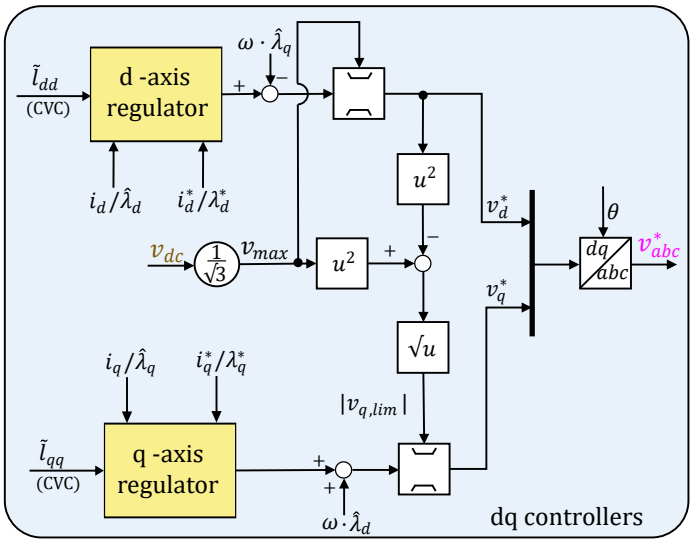


Fig. 23: Schematic view of the dq-frame based TCAs.

F. Rotor current regulator

The rotor current control is performed by employing a conventional PI regulator whose voltage margins are limited between v_{dc} and zero if a unipolar exciter is used. Alternatively, the lower voltage limit is set to $-v_{dc}$ if a full-bridge converter is employed to feed the rotor. The PI gains are tuned according to the estimation of the rotor equivalent differential inductance $\tilde{l}_{eq,f}$ (see Fig. 9), accounting, in this way, for the machine magnetic saturation (5). Compensating the voltage drop on the rotor resistance $\tilde{R}_f$ is recommended (see Fig. 24). More details about the preliminary computation of the PI gains for the rotor current control are reported in Appendix.

IV. Experimental validation

The experimental validation of the proposed torque controller has been carried out using as machine under test (MUT) a commercial sample of the EESM employed in the Renault

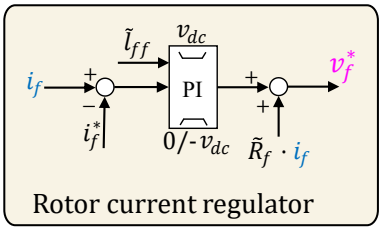


Fig. 24: Schematic view of the rotor current regulator.



Fig. 25: Sample of the Renault Zoe R135 EESM [31].

Zoe EV R135 (see Fig. 25), whose primary data are listed in TABLE I and constructional details are reported in Table II and shown in Fig. 26. Further details can be found in [44].

A. Test rig

The MUT has been operated in torque control mode, with its rotor shaft mechanically coupled to a driving machine (DM) that acted as a speed-controlled prime mover, as depicted in Fig. 27. To monitor the torque and assess the performance of the proposed UTC, a high-precision T12HP torque transducer from HBK has been installed between the MUT and the DM.

The MUT's stator has been powered by an insulated gate bipolar transistor (IGBT)-based inverter, rated for 750 V, 800 A. The inverter has been supplied at a nominal dc-link voltage of 350 V, provided by a bidirectional dc power source. The inverter operated at a constant switching frequency of 10 kHz with a dead time of 1 μs. The rotor has been fed by a dedicated SiC-based power module, configured as a full-bridge [45]. The rotor excitation converter operated at the same dc-link voltage of 350 V and a switching frequency of 20 kHz.

The control system architecture involved two distinct digital controllers. The stator inverter has been controlled by a dSPACE MicroLabBox control unit, which was responsible for executing the main control algorithm, generating PWM signals, and managing system measurements. The rotor excitation converter has been controlled by a dedicated embedded control board mounted on top of the power stage. This board was equipped with an STM32G4 microcontroller unit (MCU), which handled local current measurements, PWM generation for the SiC power switches, and communication with the main controller. The rotor current reference i_f^* and the proportional gain of the rotor current PI regulator, both computed by the main controller, have been transmitted via a CAN bus interface to the rotor MCU. It is highlighted that the delay in the CAN communication between stator and rotor digital controllers does not allow the feedforward compensation of the additive

TABLE I: Primary data of the EESM under test.

Pole number	4
Peak power	100 kW
Peak torque	245 Nm
Rated power	51 kW
Rated torque	120 Nm
Maximum speed	11000 r/min
Rated dc-link voltage	350 V
Maximum flux ($\lambda_{\max}$)	0.24 Vs
Peak stator current ($i_{\max}$)	385 A
Peak rotor current ($i_{f,\max}$)	15 A

TABLE II: Design data of the EESM under test.

Number of stator slots	48
Slots per pole and per phase	4
Number of conductors in one slot	108
Number of external parallels	4
Number of internal parallels	12
Machine axial length	175.0 mm
Stator outer diameter	262.2 mm
Stator inner diameter	156.2 mm
Rotor outer diameter	154.6 mm
Rotor inner diameter	41.0 mm

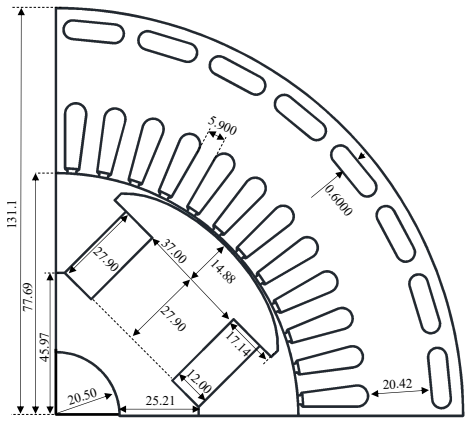


Fig. 26: Dimensions of the EESM under test (quotes in mm).

disturbance due to the cross-coupling terms (5) in the rotor current i_f control loop. The control algorithm has been entirely developed in MATLAB/Simulink, leveraging the automatic C-code generation capabilities of the dSPACE platform. Sampling frequencies of 10 kHz and 20 kHz have been adopted for the stator and rotor control loops, respectively.

Due to mechanical constraints inherent to the test rig, the maximum torque and speed of the MUT have been limited to 150 Nm and 10000 r/min, respectively. Despite these limitations, the system was capable of operating in the high-power region of the EESM, enabling the MUT to reach its peak power of 100 kW.

B. Experimental results

The proposed torque controller has been experimentally validated through a comprehensive set of tests finalized to assess its performance according to the following goals.

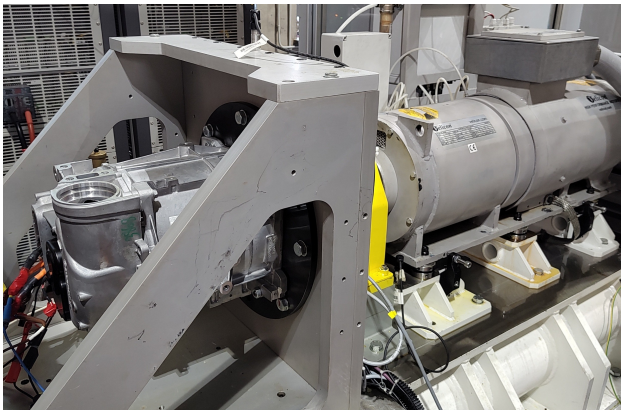


Fig. 27: View of the test rig: EESM under test (left), driving machine (right).

- Evaluation of the controller's capability to manage high torque and power conditions in the entire speed range, including deep FW scenarios.
- Verification of high dynamic performance of torque regulation across the entire speed range of the MUT.
- Assessment of the accuracy of torque regulation, including proper reference limitation according to voltage and current constraints and minimization of steady-state torque error.

In line with these objectives, the following experimental tests have been performed:

1) Maximum torque per speed (MTPS) profile
2) Fast torque reversals
3) Steady-state torque accuracy

All tests have been conducted using the TCAs discussed in this article: DFVC, DTC, FPC, CVC, and FVC. PI regulators have been employed, and for all controllers except CVC, the theoretical small-signal bandwidth of the stator control loops has been set to 200 Hz, while the rotor current control bandwidth has been set to 400 Hz. Due to the strong mutual coupling between the stator d-axis and the rotor excitation axis in the CVC strategy, tuning of the PI controllers becomes significantly more complex. To avoid instability and high-frequency noise in the torque response, the stator and rotor current control loop bandwidths for CVC have been limited to 50 Hz and 100 Hz, respectively. For each PI regulator, the theoretical phase margin has been set to 60 degrees. It is highlighted that the derating of the regulation bandwidth of the inner control loops has been applied only to CVC, since the other TCAs are ruled by state-space equations that are quite decoupled, thereby mitigating (DTC and DFVC) or avoiding (FPC and FVC) the interaction between the PI regulators of the inner control loops. The observer gain g has been set to 20 Hz, while the voltage margin factor used for flux weakening has been set at $k_{\text{fw}} = 0.9$.

The employed LUTs have been computed from the experimentally derived current-to-flux maps of the EESM under test [42], [43]. However, in case FEA-based maps are employed, discrepancies between FEA-based and real maps directly affect the torque control accuracy of TCAs using LUT9, i.e., CVC, FVC, and FPC. In this scenario, a possible solution to improve torque accuracy may consist of implementing error-compensating mechanisms developed for PMSM drives, e.g., the one reported in [46].

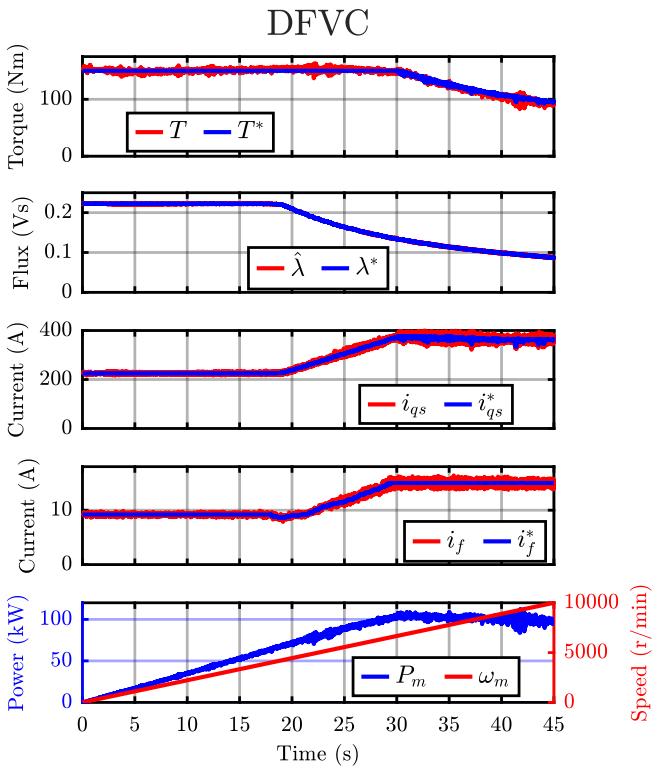


Fig. 28: MTPS profiles with DFVC: experimental results.

In this work, the LUTs have been discretized as follows: rotor current i_f from 0 to 15 A ($i_{f,\text{max}}$) with 1 A step, 16 points (pt); flux limit λ_{lim} from 0 to 0.24 Vs (λ_{max}) with 0.01 Vs step, 25 pt; finally all the pu quantities ($T_{\text{pu}}, T_{f,\text{pu}}$) from 0 to 1 with a 0.1 step, 11 pt. Therefore, the dimensions of the LUTs were: LUT1 25×1, LUT2 25×16, LUT3 25×16, LUT4 16×11, LUT5 25×11, LUT6 16×25, LUT7 16×25, LUT8 11×16, LUT9 11×11×16. The total memory required for the LUTs is approximately 1 MB. Without any computational optimization of the generated C code, the control algorithm achieved an execution time of 35 μs on the dSPACE platform, which ensures a one sampling time step of command execution delay. Consequently, the implementation of the proposed torque controller is also feasible on automotive-grade MCUs. It is highlighted that lower-resolution settings are allowed for most of the proposed LUTs. Indeed, the torque accuracy relies on LUT9 for all TCAs except DFVC and DTC. Therefore, only LUT9 should be prioritised if memory-saving optimization procedures become necessary.

1) MTPS profile: Starting from standstill, the speed of the MUT has been progressively increased from zero to the mechanical speed limit of the test rig, i.e., 10000 r/min. This was achieved by using the DM as a prime mover, imposing a constant acceleration of approximately 230 r/min/s. This speed profile was intentionally designed to approximate quasi-steady-state conditions. Simultaneously, the reference input

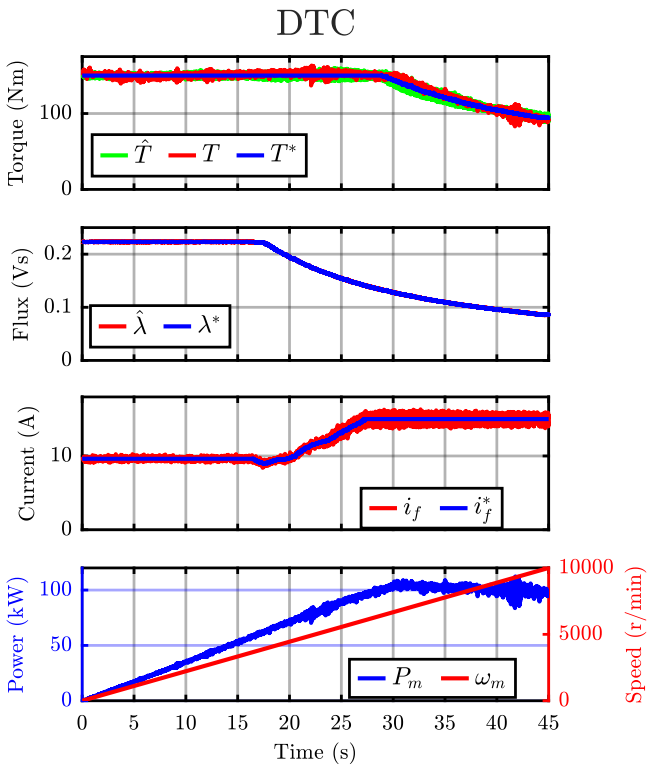


Fig. 29: MTPS profiles with DTC: experimental results.

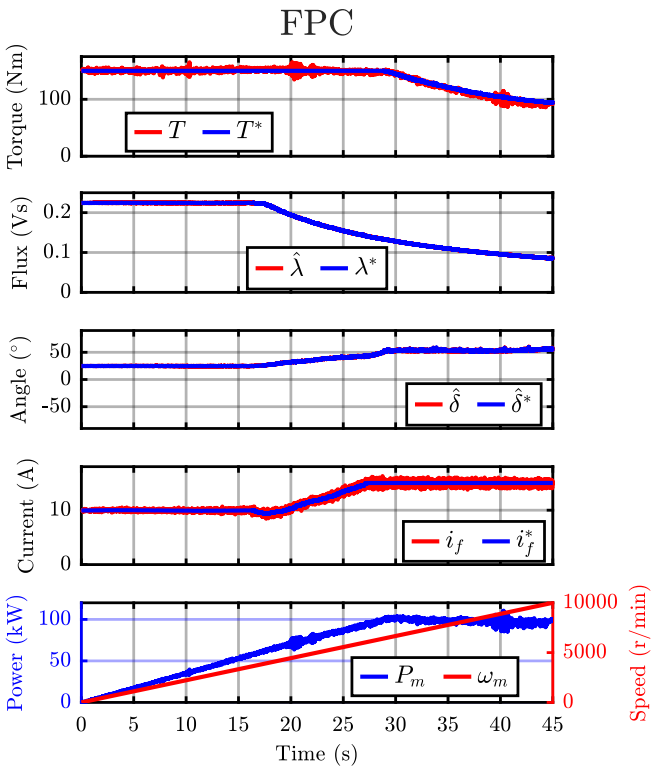


Fig. 30: MTPS profiles with FPC: experimental results.

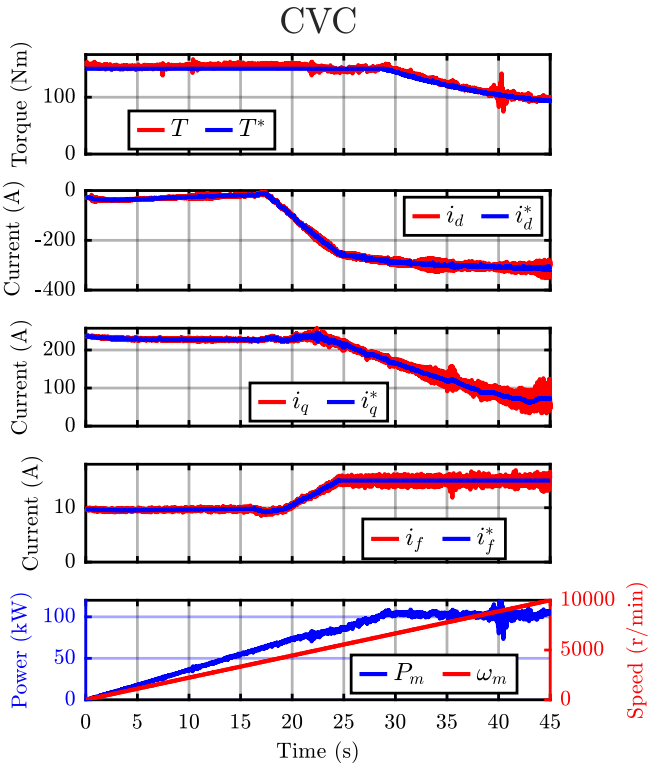


Fig. 31: MTPS profiles with CVC: experimental results.

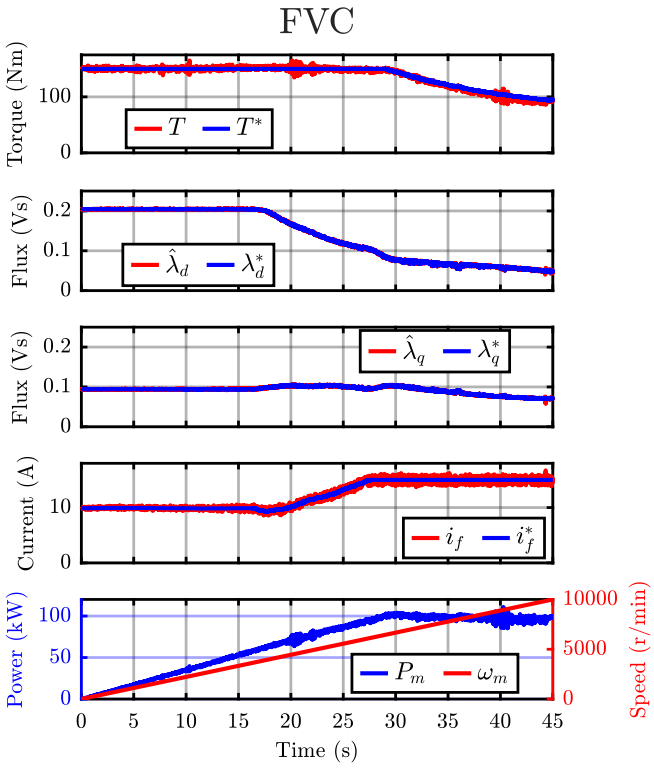


Fig. 32: MTPS profiles with FVC: experimental results.

torque T_{in}^* provided to the MUT's controller has been set to the maximum admissible value of 150 Nm. The resulting MTPS profiles of all the TCAs' regulated quantities are illustrated in Figs. 28 - 32, where the mechanical power P_m is derived from the product of torque and speed measurements acquired through the torque sensor. The results clearly demonstrate that,

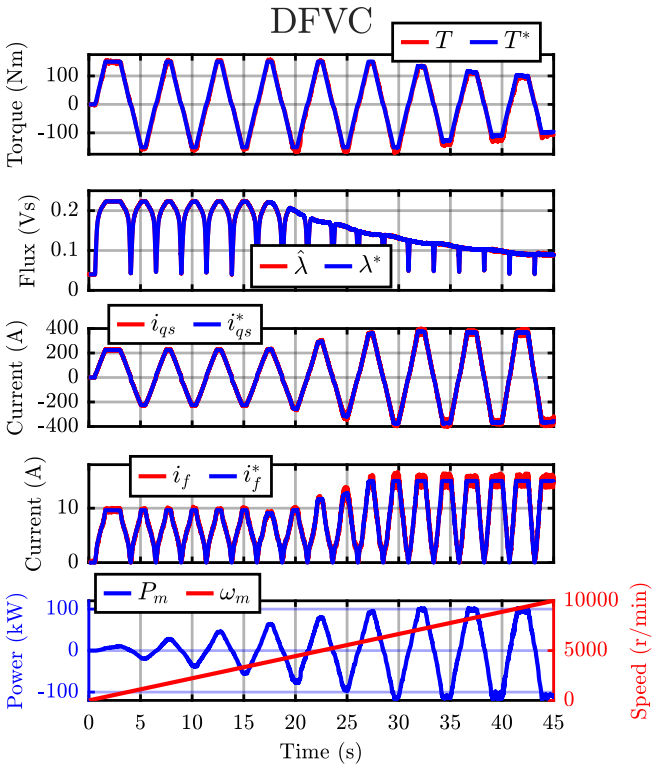


Fig. 33: Fast torque reversals along the MTPS profile with DFVC: experimental results.

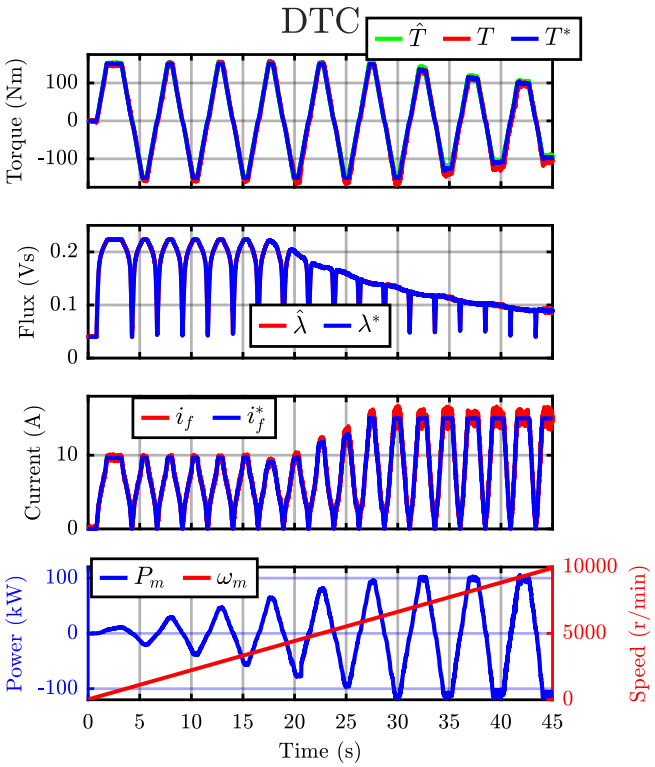


Fig. 34: Fast torque reversals along the MTPS profile with DTC: experimental results.

irrespective of the TCA chosen, the proposed torque controller successfully enables full utilization of the MUT's torque and power capability across the entire speed range. Furthermore, the stator and rotor quantities are effectively regulated in compliance with the total copper loss minimization strategy. This confirms the controller's ability to coordinate multiple constraints while ensuring energy-efficient operation.

2) Fast torque reversals: To assess the dynamic performance of the torque regulation, fast torque reversal tests have been conducted along the MTPS profile. As in the previous experiment, the MUT has been accelerated from standstill to the maximum speed of 10000 r/min using the DM, with an imposed acceleration of approximately 230 r/min/s. During this speed ramp, the input torque reference T_{in}^* has been set to its maximum value of 150 Nm. However, in contrast to the previously described test, the torque reference has been periodically reversed to introduce rapid transitions between motoring and braking modes. The reversal frequency and torque slew rate have been selected based on the mechanical constraints of the test rig and have been set to 0.5 Hz and 150 Nm/s, respectively. These values were used for all TCAs, except for the CVC. Indeed, due to the significantly reduced small-signal bandwidth required for stable operation in CVC, resulting from the mutual coupling between the stator d-axis and the rotor, such torque transitions could not be sustained across the entire speed range. For this reason, in the case of CVC, the torque reversal frequency has been limited to 0.2 Hz, with a linearly decreasing slew rate from 150 Nm/s at standstill to 25 Nm/s at 10000 r/min.

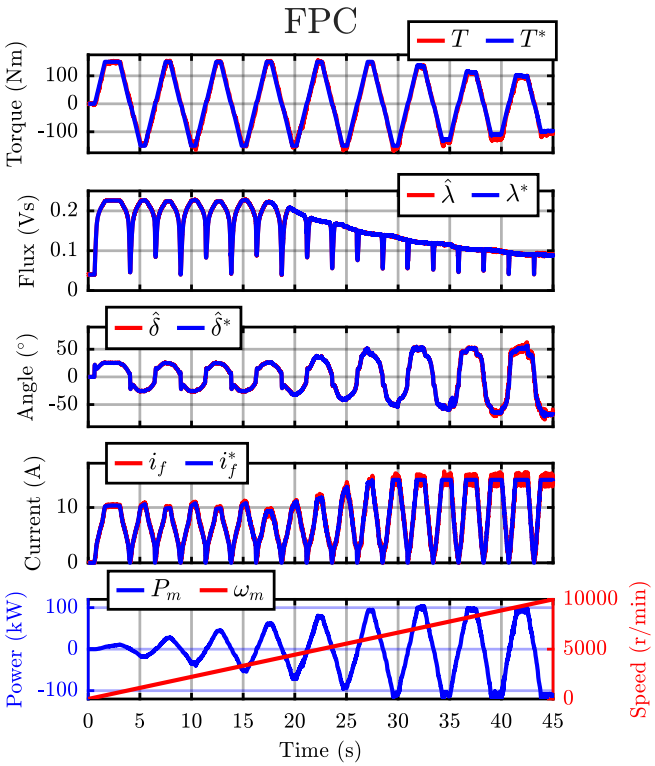


Fig. 35: Fast torque reversals along the MTPS profile with FPC: experimental results.

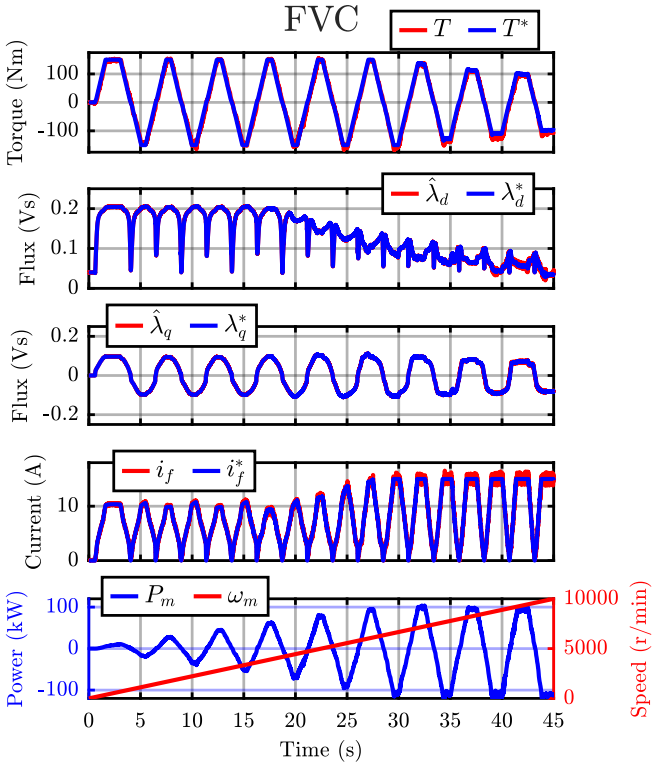


Fig. 36: Fast torque reversals along the MTPS profile with FVC: experimental results.

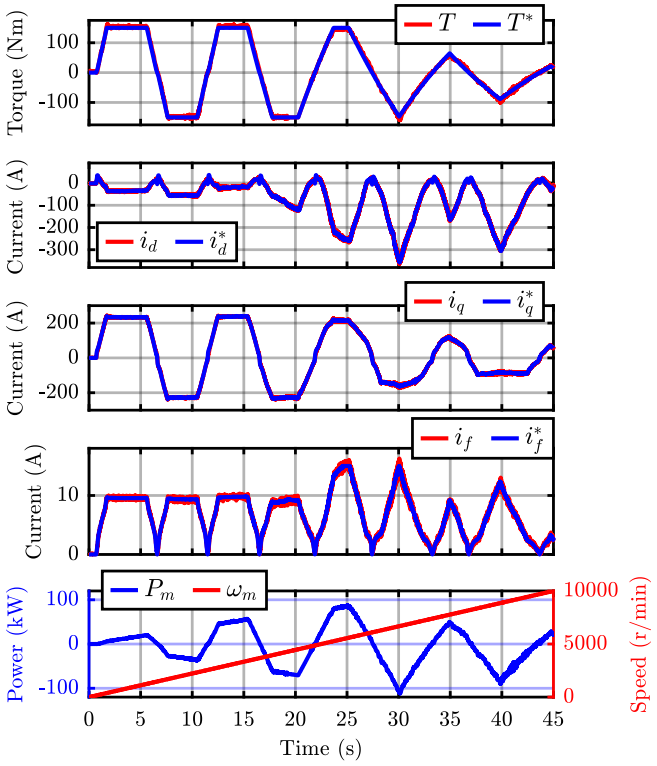


Fig. 37: Fast torque reversals along the MTPS profile with CVC: experimental results.

This dynamic stress test effectively evaluates both motoring and braking performance of the MUT while following the MTPS trajectory. It also serves to validate the robustness of the proposed torque controller, confirming its ability to handle rapid torque transitions between opposing operating modes throughout the whole speed range. The experimental results, shown in Figs. 33 - 36, indicate that all stator and rotor control variables are properly regulated under all tested conditions, including fast torque reversals in the deep FW region. No instability or overcurrent events were observed during the experimental tests, thereby demonstrating the high dynamic capability of the proposed control scheme. Nonetheless, as illustrated in Fig. 37, the CVC strategy exhibits a noticeably reduced torque dynamic response, justified by its limited control bandwidth.

3) Steady-state torque accuracy: The steady-state accuracy of the proposed torque controller has been extensively validated. To this end, a series of tests has been performed across the entire speed range of the MUT. The speed has been varied in increments of 500 r/min, from standstill up to the maximum test rig limit. At each speed level, ten equally spaced torque setpoints have been applied, spanning from zero up to the maximum allowable torque in motoring operation.

The experimental results, presented in Fig. 38, demonstrate the accuracy of the torque controller, independently of TCA. Specifically, the torque error ΔT, evaluated both in absolute terms and as a percentage of the torque limit T_{lim}, remains consistently acceptable across the tested operating range for all TCAs. These results confirm the high fidelity of the proposed controller in tracking the reference torque T^* under steady-state conditions, despite the fact that iron and mechanical losses have not been explicitly compensated in the computation of the stator flux amplitude reference λ^* and rotor current reference i_f^*. It is noted that the CVC strategy exhibits a higher torque regulation error compared to the other TCAs at speeds exceeding the base one, as illustrated in Fig. 38. This deviation arises because the dq currents imposed by the CVC do not correspond to the actual flux-generating and torque-producing components, primarily due to the unmodeled influence of iron losses. As these losses scale with frequency, their impact becomes increasingly significant at higher speeds. On the other hand, the other control strategies, DFVC, DTC, FPC, and FVC, demonstrate improved robustness against such effects. This is attributed to the direct control of the flux amplitude (DFVC and DTC) or even the stator flux vector (FVC and FPC), whose estimate is derived from the VI estimator of the flux observer which accounts for the iron losses. As a result, the flux-controlling approaches inherently incorporate the impact of iron losses, thereby enhancing torque accuracy without requiring explicit iron loss compensation.

V. Conclusion

This article proposed a unified high-performance torque controller for traction-oriented EESMs. The proposed controller enables linear torque regulation across the entire torque-speed operating range by minimizing the overall copper losses comprising both stator and rotor windings. A distinctive feature of the proposed approach is its versatility, as the same

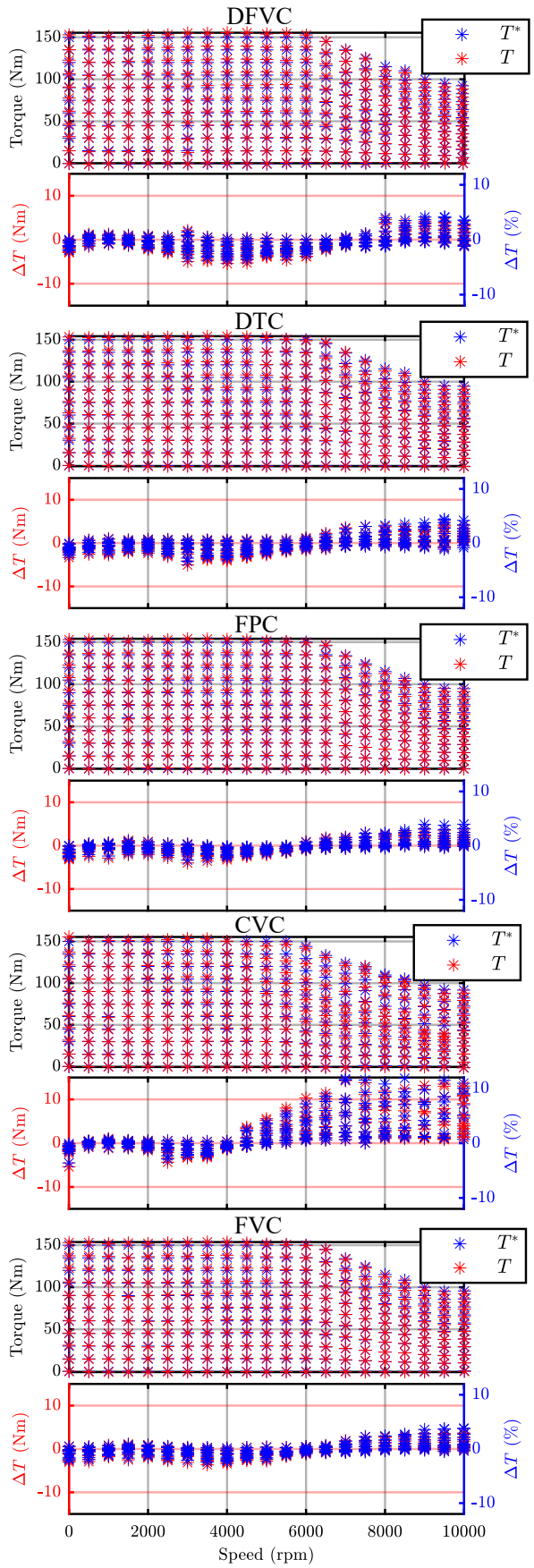


Fig. 38: Steady-state torque accuracy: experimental results.

control structure is compatible with multiple TCAs, including CVC, DFVC, DTC, FPC, and FVC. This flexibility enables the selection of the most suitable control method based on machine characteristics and application-specific requirements.

The proposed torque controller has been experimentally validated on a commercial automotive EESM. The results confirm the feasibility of the approach in fully exploiting the high-torque and high-power operating regions of the machine, while guaranteeing excellent dynamic behavior. In particular, robust torque control performance is observed under deep FW conditions, consistently across all investigated TCAs.

The experiments conducted with CVC reveal significant performance degradation in torque regulation. This is primarily attributed to the strong cross-coupling between the stator d-axis current and the rotor excitation current regulators. Moreover, CVC exhibits a reduction in steady-state torque accuracy when iron losses become non-negligible.

In the case of DTC and DFVC, an additional control module is required to actively limit the load angle during MTPV operation to prevent the machine's pull-out. However, the main shortcoming of this control module consists of its calibration, often performed by using heuristic approaches. Conversely, CVC, FPC, and FVC inherently ensure MTPV limitation; however, they require additional LUTs to achieve torque linearization. Also, these LUTs require dedicated computation and interpolation procedures described in this article.

Finally, it is highlighted that FPC and FVC controllers do not require any calibration of the inner control loops, while still ensuring accurate, robust, and high-performance torque regulation. This advantage is pivotal in traction applications to reduce efforts and cost in performing expensive calibration procedures.

ACKNOWLEDGMENT

The authors would like to acknowledge the financial support from the Power Electronics Innovation Center (PEIC) of Politecnico di Torino (www.peic.polito.it).

APPENDIX

The detailed description of how the PI regulators for flux and current control can be tuned is reported hereafter. It is highlighted that this discussion on PI regulators tuning is valid in any reference frame and for any axis. The subscript "x" is used to identify a generic axis.

1) Flux controller design: The simplified flux control loop in the Laplace domain is illustrated in Fig. 39. The inverter is modeled as a delay element with unitary gain, which can be approximated by a first-order transfer function as follows:

$$H_{\text{inv}}(s) \simeq \frac{1}{1 + s \cdot \tau_d} = 1.5 \cdot T_s, \tag{36}$$

where T_s denotes the switching period, assumed to be equal to the sampling period (single-edge PWM is considered). Assuming accurate voltage reconstruction, the observer can

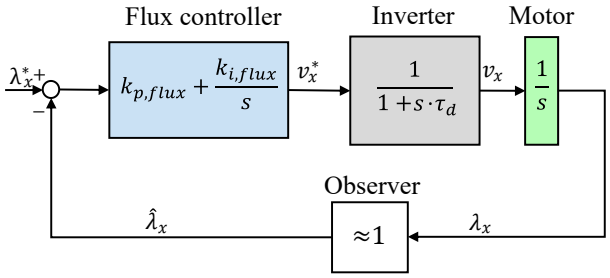


Fig. 39: Flux control scheme in Laplace domain.

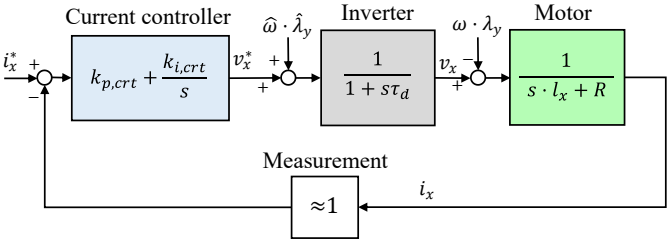


Fig. 40: Current control scheme in Laplace domain.

be approximated as a unity gain. Consequently, the open-loop transfer function of the flux control loop is expressed as:

$$H_{\text{OL,flux}}(s) = \left(k_{p,\text{flux}} + \frac{k_{i,\text{flux}}}{s}\right) \cdot \frac{1}{s} \cdot \frac{1}{1+s\cdot\tau_d} = k_{p,\text{flux}} \cdot \frac{s-\omega_{z,\text{flux}}}{s^2} \cdot \frac{1}{1+s\cdot\tau_d}, \tag{37}$$

where $\omega_{z,\text{flux}} = \frac{k_{i,\text{flux}}}{k_{p,\text{flux}}}$ represents the zero of the flux PI controller. It can be observed that the open-loop transfer function in (37) contains a zero, two poles at null frequency, and an additional high-frequency pole introduced by the inverter delay.

It is important to emphasize that the flux control loop is independent of the machine parameters and the operating point, i.e., it is not influenced by variations in torque or speed. Based on the transfer function analysis, the design of the flux controller can be summarized as follows:

- The crossover frequency $f_{c,\text{flux}}$ (in Hz) is chosen as a function of the sampling frequency. The theoretical upper limit of this frequency is determined by the inverse of the inverter delay:

$$\omega_{c,\text{flux,max}} = \tau_d^{-1} = \frac{1}{1.5\cdot T_s} = \frac{f_s}{1.5} \Rightarrow f_{c,\text{flux,max}} = \frac{f_s}{1.5\cdot 2\pi} = \frac{f_s}{3\pi} \simeq \frac{f_s}{10}. \tag{38}$$

- The controller zero $\omega_{z,\text{flux}}$ is determined to achieve the desired phase margin Φ_{PM} as

$$\omega_{z,\text{flux}} = \frac{\omega_{c,\text{flux}}}{\tan\left(\Phi_{\text{PM}} + \arctan(\omega_{c,\text{flux}}\cdot\tau_d)\right)}, \quad \Phi_{\text{PM}} + \arctan(\omega_{c,\text{flux}}\cdot\tau_d) < 90^\circ. \tag{39}$$

- The integral gain is obtained as in [21]:

$$k_{i,\text{flux}} = \omega_{c,\text{flux}}^2 \cdot \sqrt{\frac{1+(\tau_d\cdot\omega_{c,\text{flux}})^2}{1+(\frac{\omega_{c,\text{flux}}}{\omega_{z,\text{flux}}})^2}}. \tag{40}$$

- The proportional gain of the flux controller is finally obtained as

$$k_{p,\text{flux}} = \frac{k_{i,\text{flux}}}{\omega_{z,\text{flux}}}. \tag{41}$$

2) Current controller design: The simplified control loop in the Laplace domain is shown in Fig. 40. In contrast to the flux loop, the current control loop depends explicitly on the machine parameters. Assuming that the current measurement delay is negligible, the feedback block can be approximated by a unity gain. Thus, the open-loop transfer function of the current controller is given by

$$H_{\text{OL,crt}}(s) = \left(k_{p,\text{crt}} + \frac{k_{i,\text{crt}}}{s}\right) \cdot \frac{1}{1+s\cdot\tau_d} \cdot \frac{1}{R+s\cdot l_x} = k_{p,\text{crt}} \cdot \frac{s+\omega_{z,\text{crt}}}{s} \cdot \frac{1/l_x}{s+\frac{R}{l_x}} \cdot \frac{1}{1+s\cdot\tau_d}. \tag{42}$$

Applying the zero–pole cancellation method, the controller zero is selected to cancel the dominant pole of the motor, leading to

$$\omega_{z,\text{crt}} = \frac{R}{l_x} \Rightarrow \frac{k_{i,\text{crt}}}{k_{p,\text{crt}}} = \frac{R}{l_x} \Rightarrow k_{i,\text{crt}} = k_{p,\text{crt}} \cdot \frac{R}{l_x}. \tag{43}$$

Substituting (43) into the open-loop transfer function yields

$$H_{\text{OL,crt}}(s) = \frac{k_{p,\text{crt}}}{l_x} \cdot \frac{1}{s} \cdot \frac{1}{1+s\cdot\tau_d}. \tag{44}$$

The open-loop transfer function in (44) features one pole at null frequency and one high-frequency pole introduced by the inverter delay. The current controller design can be summarized as follows:

- A typical phase margin of $\Phi_{\text{PM}} = 60^\circ$ is selected. The crossover frequency $\omega_{c,\text{crt}}$ is then determined as:

$$\omega_{c,\text{crt}} = \frac{\tan(90^\circ - \Phi_{\text{PM}})}{\tau_d}. \tag{45}$$

- The proportional gain is computed as:

$$k_{p,\text{crt}} = \omega_{c,\text{crt}} \cdot l_x. \tag{46}$$

- The integral gain is derived as:

$$k_{i,\text{crt}} = k_{p,\text{crt}} \cdot \omega_{z,\text{crt}} = k_{p,\text{crt}} \cdot \frac{R}{l_x}. \tag{47}$$

From (46) and (47), it is evident that the current controller parameters depend on the machine resistance R and the corresponding differential inductance l_x. The value of l_x changes with the operating point, as it is a function of i_d, i_q, and i_f. The rotor field current i_f significantly influences the magnetic behavior of the machine; thus, it is impractical to assume a fixed value for l_x. Instead, a real-time estimation $\hat{l}_x$ is computed based on the current-to-flux relationships, as

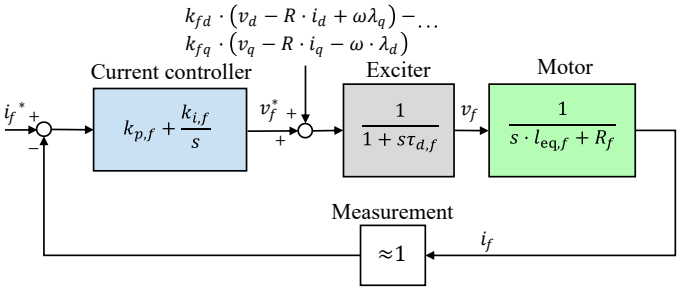


Fig. 41: Rotor field current control scheme in Laplace domain.

depicted in Fig. 4. Regarding the dependency of the stator resistance due to the temperature effects, a simplified but robust approach consist of considering its rated value.

3) Rotor field current controller design: The design methodology of the rotor field current controller mirrors that employed for the stator current controller. The same analytical framework can be applied by substituting the stator parameters R and l_x with their corresponding rotor quantities, namely the rotor resistance R_f and the rotor inductance $l_{eq,f}$. This last is also estimated in real time using the current-to-flux relationships, as depicted in Fig. 4. Furthermore, the disturbance term is not anymore due to the back-emf but is caused by the cross-coupling terms, as illustrated in Fig. 41. Consequently, the same tuning procedure can be adopted to determine the proportional and integral gains of the rotor field current controller.

REFERENCES

[1] A. El-Refaie and M. Osama, "High specific power electrical machines: A system perspective," *CES Transactions on Electrical Machines and Systems*, vol. 3, no. 1, pp. 88–93, 2019.

[2] C. Rossi, D. Casadei, A. Pilati, and M. Marano, "Wound rotor salient pole synchronous machine drive for electric traction," in *Conference Record of the 2006 IEEE Industry Applications Conference Forty-First IAS Annual Meeting*, vol. 3, 2006, pp. 1235–1241.

[3] F. Graffeo, S. Vaschetto, M. Cossale, M. Kerschbaumer, E. C. Bortoni, and A. Cavagnino, "Cylindrical wound-rotor synchronous machines for traction applications," in *2020 International Conference on Electrical Machines (ICEM)*, vol. 1, 2020, pp. 1736–1742.

[4] F. Graffeo, S. Vaschetto, A. Tenconi, and A. Cavagnino, "No-load characteristic computation for wound field synchronous propulsion motors," in *2023 IEEE International Conference on Electrical Systems for Aircraft, Railway, Ship Propulsion and Road Vehicles and International Transportation Electrification Conference (ESARS-ITEC)*, 2023, pp. 1–6.

[5] ——, "Fast sizing procedure for salient-pole wound field synchronous motors for transportation electrification," in *2023 IEEE International Electric Machines and Drives Conference (IEMDC)*, 2023, pp. 1–7.

[6] M. Märgner and W. Hackmann, "Control challenges of an externally excited synchronous machine in an automotive traction drive application," in *2010 Emobility - Electrical Power Train*, 2010, pp. 1–6.

[7] R. Breda, E. Colavitto, S. Calligaro, R. Petrella, and B. Sarlioglu, "Model predictive control for wound rotor synchronous machines based on closed-form solution and fixed switching frequency," in *2024 IEEE Energy Conversion Congress and Exposition (ECCE)*, 2024, pp. 6349–6356.

[8] R. Breda, G. Andrioli, S. Calligaro, and R. Petrella, "Extended mtpa and flux-weakening control with total copper loss minimisation and transient torque compensation for wound-rotor synchronous machines," in *2023 IEEE Energy Conversion Congress and Exposition (ECCE)*, 2023, pp. 4829–4836.

[9] R. Breda, N. Andreon, S. Calligaro, and R. Petrella, "Comprehensive flux-weakening and analytical extended mtpa control featuring transient torque compensation for hybrid excited synchronous machines," in *2024 IEEE Energy Conversion Congress and Exposition (ECCE)*, 2024, pp. 6417–6424.

[10] L. Geier, S. Goehner, J. Stoss, A. Liske, and M. Hiller, "A novel highly dynamic torque control scheme for electrically excited synchronous machines," in *2024 IEEE 9th Southern Power Electronics Conference (SPEC)*, 2024, pp. 1–7.

[11] K. D. Hoang and H. K. A. Aorith, "Online control of ipmsm drives for traction applications considering machine parameter and inverter nonlinearities," *IEEE Transactions on Transportation Electrification*, vol. 1, no. 4, pp. 312–325, 2015.

[12] H. A. A. Awan, Z. Song, S. E. Saarakkala, and M. Hinkkanen, "Optimal torque control of saturated synchronous motors: Plug-and-play method," *IEEE Transactions on Industry Applications*, vol. 54, no. 6, pp. 6110–6120, 2018.

[13] E. Trancho, E. Ibarra, A. Arias, C. Salazar, I. Lopez, A. D. de Guereñu, and A. Peña, "Ipmsm torque control strategies based on luts and vct feedback for robust control under machine parameter variations," in *IECON 2016 - 42nd Annual Conference of the IEEE Industrial Electronics Society*, 2016, pp. 2833–2838.

[14] V. Manzolini, D. Da Rù, and S. Bolognani, "An effective flux weakening control of a syrm drive including mtpv operation," *IEEE Transactions on Industry Applications*, vol. 55, no. 3, pp. 2700–2709, 2019.

[15] I. Boldea, M. C. Paicu, and G.-D. Andreescu, "Active flux concept for motion-sensorless unified ac drives," *IEEE Transactions on Power Electronics*, vol. 23, no. 5, pp. 2612–2618, 2008.

[16] T. Habetler, F. Profumo, M. Pastorelli, and L. Tolbert, "Direct torque control of induction machines using space vector modulation," *IEEE Transactions on Industry Applications*, vol. 28, no. 5, pp. 1045–1053, 1992.

[17] C. Lascu, I. Boldea, and F. Blaabjerg, "A modified direct torque control for induction motor sensorless drive," *IEEE Transactions on Industry Applications*, vol. 36, no. 1, pp. 122–130, 2000.

[18] G. Pellegrino, R. Bojoi, and P. Guglielmi, "Unified direct-flux vector control for ac motor drives," *IEEE Transactions on Industry Applications*, vol. 47, no. 5, pp. 2093–2102, 2011.

[19] S. Rubino, R. Bojoi, E. Armando, and A. Tenconi, "Deadbeat direct flux vector control of surface permanent magnet motor drives," *IEEE Transactions on Industry Applications*, vol. 56, no. 3, pp. 2685–2699, 2020.

[20] H. A. A. Awan, M. Hinkkanen, R. Bojoi, and G. Pellegrino, "Stator-flux-oriented control of synchronous motors: A systematic design procedure," *IEEE Transactions on Industry Applications*, vol. 55, no. 5, pp. 4811–4820, 2019.

[21] S. Rubino, L. Tolosano, F. Mandrile, E. Armando, and R. Bojoi, "Flux polar control (fpc): A unified torque controller for ac motor drives," *IEEE Transactions on Industry Applications*, vol. 59, no. 4, pp. 4140–4163, 2023.

[22] H. A. A. Awan, S. E. Saarakkala, and M. Hinkkanen, "Flux-linkage-based current control of saturated synchronous motors," *IEEE Transactions on Industry Applications*, vol. 55, no. 5, pp. 4762–4769, 2019.

[23] G. Friedrich, "Comparative study of three control strategies for the synchronous salient poles and wound rotor machine in automotive applications with on board energy," in *1994 Fifth International Conference on Power Electronics and Variable-Speed Drives*, 1994, pp. 706–709.

[24] C. D. Nguyen and W. Hofmann, "Self-tuning adaptive copper-losses minimization control of externally excited synchronous motors," in *2014 International Conference on Electrical Machines (ICEM)*, 2014, pp. 897–902.

[25] C. Zaghrini, G. Khoury, M. Fadel, R. Ghosn, and F. Khatounian, "Minimum copper losses per torque optimization on electrically excited synchronous motors for electric vehicles applications," in *2022 IEEE 20th International Power Electronics and Motion Control Conference (PEMC)*, 2022, pp. 661–666.

[26] A. K. Jain and V. T. Ranganathan, "Modeling and field oriented control of salient pole wound field synchronous machine in stator flux coordinates," *IEEE Transactions on Industrial Electronics*, vol. 58, no. 3, pp. 960–970, 2011.

[27] Y. Nie, I. P. Brown, and D. C. Ludois, "Deadbeat-direct torque and flux control for wound field synchronous machines," *IEEE Transactions on Industrial Electronics*, vol. 65, no. 3, pp. 2069–2079, 2018.

[28] Y. Nie, D. C. Ludois, and I. P. Brown, "Deadbeat-direct torque and flux control of wound field synchronous machine at low sampling to fundamental frequency ratios," *IEEE Transactions on Industry Applications*, vol. 55, no. 4, pp. 3813–3822, 2019.

[29] Y. Kim and K. Nam, "Copper-loss-minimizing field current control scheme for wound synchronous machines," *IEEE Transactions on Power Electronics*, vol. 32, no. 2, pp. 1335–1345, 2017.

[30] M.-R. Park, D.-M. Kim, Y.-H. Jung, M.-S. Lim, and J.-P. Hong, "Modeling, design and control of wound-field synchronous motor for high energy efficiency of electric vehicle," in *2019 IEEE Energy Conversion Congress and Exposition (ECCE)*, 2019, pp. 3960–3967.

[31] F. Graffeo, S. Rubino, M. J. Molina, S. Vaschetto, and A. Tenconi, "Efficiency mapping of electrically excited synchronous motors with different control strategies," in *2025 IEEE Workshop on Electrical Machines Design, Control and Diagnosis (WEMDCD)*, 2025, pp. 1–6.

[32] A. Ionta, S. Rubino, F. Mandrile, F. Graffeo, R. Bojoi, and E. Armando, "Direct flux vector control of electrically excited synchronous machines for electrical vehicles," in *2024 IEEE Energy Conversion Congress and Exposition (ECCE)*, 2024, pp. 6431–6438.

[33] H. Eldeeb, C. M. Hackl, L. Horlbeck, and J. Kullick, "A unified theory for optimal feedforward torque control of anisotropic synchronous machines," *International Journal of Control*, vol. 91, no. 10, pp. 2273–2302, 2018.

[34] A. Ionta, S. Rubino, F. Graffeo, and R. Bojoi, "Unified torque control of electrically excited synchronous machines for traction applications," in *2025 IEEE Industry Applications Society Annual Meeting (IAS)*, 2025, pp. 1–8.

[35] S.-K. Sul, *Control of Electric Machine Drive Systems*. New York, NY, USA: Wiley-IEEE Press, 2011.

[36] B. Stumberger, G. Stumberger, D. Dolinar, A. Hamler, and M. Trlep, "Evaluation of saturation and cross-magnetization effects in interior permanent-magnet synchronous motor," *IEEE Transactions on Industry Applications*, vol. 39, no. 5, pp. 1264–1271, 2003.

[37] A. Hava, R. Kerkman, and T. Lipo, "Simple analytical and graphical methods for carrier-based pwm-vsi drives," *IEEE Transactions on Power Electronics*, vol. 14, no. 1, pp. 49–61, 1999.

[38] A. Vagati, M. Pastorelli, G. Franceschini, and V. Drogoreanu, "Flux-observer-based high-performance control of synchronous reluctance motors by including cross saturation," *IEEE Transactions on Industry Applications*, vol. 35, no. 3, pp. 597–605, 1999.

[39] G. Pellegrino, R. I. Bojoi, P. Guglielmi, and F. Cupertino, "Accurate inverter error compensation and related self-commissioning scheme in sensorless induction motor drives," *IEEE Transactions on Industry Applications*, vol. 46, no. 5, pp. 1970–1978, 2010.

[40] I. Bojoi, E. Armando, G. Pellegrino, and S. Rosu, "Self-commissioning of inverter nonlinear effects in ac drives," in *2012 IEEE International Energy Conference and Exhibition (ENERGYCON)*, 2012, pp. 213–218.

[41] S.-Y. Kim, C. Choi, K. Lee, and W. Lee, "An improved rotor position estimation with vector-tracking observer in pmsm drives with low-resolution hall-effect sensors," *IEEE Transactions on Industrial Electronics*, vol. 58, no. 9, pp. 4078–4086, 2011.

[42] E. Armando, R. Bojoi, P. Guglielmi, G. Pellegrino, and M. Pastorelli, "Experimental identification of the magnetic model of synchronous machines," *IEEE Transactions on Industry Applications*, vol. 49, no. 5, pp. 2116–2125, 2013.

[43] S. Goehner, J. Stoss, M. Brodatzki, B. Bachowsky, A. Liske, J. Kolb, and M. Hiller, "Combining locked rotor and steady state tests for eesm flux linkage identification," in *2024 IEEE 9th Southern Power Electronics Conference (SPEC)*, 2024, pp. 1–6.

[44] F. Graffeo, S. Ferrari, S. Rubino, S. Vaschetto, and G. Pellegrino, "A scaling procedure for electrically-excited synchronous machines utilizing flux and loss maps," in *2024 International Conference on Electrical Machines (ICEM)*, 2024, pp. 1–8.

[45] F. Stella, S. Rubino, E. Vico, R. Bojoi, and E. Armando, "Excitation sic converter for electrically excited traction synchronous motor using rotary transformer and field rotor current estimator," in *2024 IEEE Energy Conversion Congress and Exposition (ECCE)*, 2024, pp. 2000–2006.

[46] H. EL KHATIB, D. GERLING, and M. SAUR, "Deadbeat flux vector control as a one single control law operating in the linear, overmodulation, and six-step regions with time-optimal torque control," *IEEE Open Journal of Industry Applications*, vol. 3, pp. 247–270, 2022.



Alessandro Ionta (Student Member, IEEE) was born in Rome, Italy, in 1999. He received the bachelor degree in electrical engineering and the master degree in mechatronic engineering, in 2020 and 2022, respectively, from the Politecnico di Torino, Torino, Italy, where he is currently working toward the Ph.D degree with Dipartimento Energia "G. Ferraris". His Ph.D topic relates on advanced control and modeling of electrical motors for traction applications, with a particular focus on electrically excited synchronous motors.



Sandro Rubino (Senior Member, IEEE) received the M.Sc. and PhD degrees in electrical engineering from Politecnico di Torino, Torino, Italy, in 2014 and 2019, respectively. He is currently an Associate Professor at the Energy Department "G. Ferraris" of Politecnico di Torino. His research activities include modelling and controlling multiphase electrical machines and high-performance motor drives. Prof. Sandro Rubino currently serves as the Secretary of the Industrial Drive Committee (IDC) of the IEEE Industry Applications Society (IAS). Also, he is an Associate Editor of IEEE Transactions on Industry Applications and IEEE Journal of Emerging and Selected Topics in Power Electronics. Prof. Sandro Rubino received four paper awards from IAS-IDC and two PhD thesis awards for the design and validation of advanced torque controllers for traction and propulsion motors. He is involved in many research projects with industry aimed at technology transfer from academia.



Federica Graffeo (S'20–M'24) received the B.Sc. degree in energy engineering from the Università degli Studi di Palermo, Palermo, Italy, in 2017, and the M.Sc. and Ph.D. degrees in electrical engineering from the Politecnico di Torino, Turin, Italy, in 2020, and 2023, respectively. She is currently an Assistant Professor with the Dipartimento Energia "G. Ferraris," Politecnico di Torino. Her research interests include electromagnetic and thermal design of synchronous electrical machines for transportation applications, with a particular focus on wound field synchronous motors. Dr. Graffeo serves as a reviewer for some IEEE TRANSACTIONS and international conferences.



Fausto Stella is an assistant professor at Politecnico di Torino, Turin, Italy. He received both his Bachelor's and Master's degrees in Electrical Engineering from the same university in 2012 and 2015, respectively. In 2017 he was a visiting PhD student at the University of Nottingham, UK and in 2019 he received his PhD degree from the Politecnico di Torino. His research interests include the design of power electronic converters, focusing on SiC semiconductors and reliability issues, and the control of converters via embedded systems.



Radu Bojoi (Fellow, IEEE) received the M.Sc.in electrical engineering from the Technical University of Iasi, Iasi, Romania,in 1993, and the Ph.D. degree in electrical engineering from the Politecnico di Torino, Torino, Italy, in 2002. He is currently a Full Professor of Power Electronics and Electrical Drives with the Energy Department "G. Ferraris" and Chairperson of the Power Electronics Innovation Center, Politecnico di Torino. Dr. Bojoi is the recipient of ten IEEE paper awards, being co-author of more than 200 papers covering electrical drives and power electronics for industrial applications, transportation electrification, power quality, and home appliances. Prof. Bojoi is involved in many research projects with industry aiming at obtaining new products involving emerging technologies.